ULTRASONIC LABORATORY TESTS OF GEOPHYSICAL TOMOGRAPHIC RECONSTRUCTION

by

Tien-when Lo

B.S. National Taiwan University

(1980)

SUBMITTED TO THE DEPARTMENT OF EARTH, ATMOSPHERIC, AND PLANETARY SCIENCES IN PARTIAL FULFILLMENT OF THE REQUIREMENTS FOR THE DEGREE OF

MASTER OF SCIENCE

at the

August 30, 1986

Signature of Author .....
Department of Earth, Atmospheric, and Planetary Sciences
August, 1986

Certified by .....
M. Nafi Toksöz
Thesis Advisor

Accepted by .....
William F. Brace
Chairman
Departmental Committee on Graduate Students

ULTRASONIC LABORATORY TESTS OF GEOPHYSICAL TOMOGRAPHIC RECONSTRUCTION

by

Tien-when Lo

Submitted to the Department of Earth, Atmospheric and Planetary Sciences on August 30, 1986, in partial fulfillment of the requirements for the degree of Master of Science.

ABSTRACT

Various geophysical tomographic imaging techniques are tested in our ultrasonics laboratory. We evaluate these imaging techniques from three viewpoints. First, we compare the diffraction tomography with ART. The items we compared include the effect of incomplete illumination of the object by the insonifying waves and the different adaptabilities of these two techniques on objects with various size and acoustic properties. Second, we compared the reconstructions based on the Born and the Rytov approximations for diffraction tomography. Finally, we test the multi-source and multi-frequency holography for imaging small but strong scatterers. Our experimental results indicate that: (1) When scattered field can be obtained, geophysical diffraction tomography is in general superior to the ART because the geophysical diffraction tomography is less restricted by incomplete illumination and can image small objects whose size is comparable with the wavelength. The only situation that the ART is preferred is when

both the size of the object and the acoustic impedance contrast between the object and the background medium is large. (2) The Rytov approximation is valid over a wider frequency range than the Born approximation in the cross-borehole experiment. In the VSP snd the surface reflection experiments, there is no substantial difference between images reconstructed based on these two approximation methods. (3) Multi-source holography is demonstrated to be an efficient imaging tool when the object is small and discrete.

Thesis Supervisor: M. Nafi Toksöz

Title: Professor of Geophysics

1. INTRODUCTION

Geophysical tomography has become an important research topic because of its capability of determining subsurface structures in three dimensional space from surface, borehole, and cross-hole data. In this study we conduct a set of ultrasonic model experiments to image objects with the source-receiver geometries analogous to surface reflection, vertical seismic profiling and cross-hole measurements. Using these laboratory data, we reconstruct the objects using different tomographic algorithms. We compare the results in order to determine the relative performance of different reconstruction algorithms for each geometry. The tomographic reconstruction algorithms can be classified into two categories: series expansion methods and transform methods. Censor (1983) gives a good overview of the series expansion methods such as algebraic reconstruction technique (ART) and simultaneous iterative reconstruction technique (SIRT) and claims that the series expansion methods have a wider range of applicability to scanning geometries than the transform methods do. Most geophysical tomographic studies use series expansion methods (Dines and Lytle, 1979; McMechan, 1983; Kretzschmar et al, 1984; Menke, 1984; Bishop et al, 1985; Invansson, 1985; Peterson et al, 1985; Chiu et al, 1986; Cottin et al, 1986; Invansson, 1986; Gustavsson et al, 1986; Ramirez, 1986). The other kind of reconstruction algorithms, the transform methods, are widely used in commercial CT scanner for medical imaging. Lewitt (1983) reviewed these algorithms and sub-divided them into direct Fourier inversion methods and convolution - backprojection methods. Although their reconstuction formulae look different, both the direct Fourier inversion method and convolution - backprojection method are

derived from the same starting point, the Fourier slice projection theorem (Mersereau and Oppenheim, 1974). This theorem shows that the one-dimensional Fourier transform of a "projection" is equal to a slice of the two-dimensional Fourier transform of the object. The biggest advantage of the transform methods over the series expansion methods is that they are one step inversions (do not require iterations) and therefore they are faster than ART and SIRT. The reason why transform methods are not widely used in geophysical applications are: (1) "Projection" can be obtained only in very restricted directions along the surface and the available boreholes; (2) High attenuation in earth materials force us to use insonifying waves with wavelength comparable to the size of the subsurface inhomogeneities, resulting in complex diffraction and scattering. Looking at these two difficulties, Mueller et al (1979, 1980) proposed a new transform method: diffraction tomography, which has both the speed of the transform methods and the geometrical flexibility comparable to the series expansion methods. Devany (1982, 1984), Esmersoy (1986), and Wu and Toksöz (1986) then derived the filtered - backpropagation reconstruction algorithms suited for geophysical diffraction tomography. This study tests the performance of diffraction tomography using the ultrasonic laboratory data and compares the result with reconstructions by ART using the same data set.

Besides comparing geophysical diffraction tomography with geophysical ART, this paper also takes an experimental approach to examine the fidelity of the diffraction tomography reconstructions due to limited illumination directions dictated by the source-receiver configurations. Data collected in the space-time domain cover only a portion

of the two dimensional Fourier transform of the object in the spatial frequency domain. Missing data in certain places in the spatial frequency domain will result in poor resolution in certain places in the space domain after the reconstruction. Diffraction tomography was proposed because theoretically it survives under incomplete illumination. It is important to test this endurance for different source-receiver configurations by laboratory data.

The reconstruction algorithms in diffraction tomography are derived from the wave equation which relates the object function and the scattered wavefield. In order to derive a feasible reconstruction algorithm which relates the object function and the scattered wavefield, we have to find a linear solution to a nonlinear wave equation. The two most common methods to obtain this linear solution are the Born and the Rytov approximations. The Born approximation results in a linear mapping between the object function and the complex (amplitude and phase) scattered wavefield. The Rytov approximation results in a linear mapping between the object function and the phase of the scattered wavefield. It should be noticed that although the reconstuction formula using the Born and the Rytov approximations are similar, the physical assumption behind these two approximation methods are quite different. In this paper, we will compare the diffration tomography reconstructions based on both approximation methods.

Another tomographic reconstruction technique we study in this paper is the multi-source holography. As shown by Wu and Toksöz (1986), multi-soouce holography is equivalent to diffraction tomography except that diffraction tomography filters the scattered wavefield data in the spatial frequency domain before backpropagation whereas

multi-source holography backpropagate the scattered wavefield directly without filtering. This filtering process in diffraction tomography improves the quality of the reconstructions at the price of requiring the sampling interval meet the Nyquist rate. Without this filtering, numerical experiments by Wu and Toksöz (1986) suggest that multi-source holography can still successfully reconstruct images of small, discrete objects. This argument is also tested by our ultrasonic laboratory data.

2. THE PRINCIPLES OF DIFFRACTION TOMOGRAPHY, MULTI-SOURCE HOLOGRAPHY, AND ALGEBRAIC RECONSTRUCTION TECHNIQUE (ART)

In this section we review the three imaging methods: diffraction tomography, multi-source holography, and ART. In the following we describe the basic principles of these three techniques. For a more complete derivation of these methods, the reader is referred to Dines and Lytle (1979), Kak (1985), and Wu and Toksöz (1986).

(I) Diffraction Tomography

For the derivations and the experiments we use a two-dimensional geometry for the object and geophone and source arrays as shown in Figure 1. An object with varying wave velocity $C(\underline{r})$ is situated in the background medium with a uniform velocity C_o, where $\underline{r}$ is the position vector of the object point. By the first Born approximation (see Appendix), we can obtain the Lippmann-Schwinger equation for the forward scattering problem

$$U_s(\underline{r}_g, \underline{r}_s) = -k_o^2 \int_S O(\underline{r}) G(\underline{r}, \underline{r}_s) G(\underline{r}_g, \underline{r}) d\underline{r} \tag{1}$$

where subscripts g and s refer to geophone and source respectively, $U_s(\underline{r}_g, \underline{r}_s)$ is the scattered field measured at point $\underline{r}_g$ when the point source is at $\underline{r}_s$, $O(\underline{r})$ is the object function defined as

$$O(\underline{r}) = 1 - \frac{C_o^2}{C^2(\underline{r})}. \tag{2}$$

G is the free-space Green's function for the background medium

$$G(\underline{r}\,, \underline{r}\,') = \frac{i}{4} H_o^{(1)}(k_o \mid \underline{r}\, - \underline{r}\,' \mid), \tag{3}$$

where $H_o^{(1)}$ is zero-order Hankel's function of the first kind, and $k_o = \frac{w}{C_o}$ is the wavenumber in the background medium.

Taking the Fourier transform of Equation (1) along both the source line and the geophone line, we have

$$\tilde{U}_s(k_g, k_s) = -k_o^2 \int_S O(\underline{r}\,) \tilde{G}_s(k_s, \underline{r}\,) \tilde{G}_g(k_g, \underline{r}\,) d\underline{r}\,\,, \tag{4}$$

where$\tilde{U}_s(k_g, k_s)$ is the double Fourier transform of $U_s(\underline{r}_{\,g}, \underline{r}_{\,s})$ and is defined as

$$\tilde{U}_s(k_g, k_s) = \int_{-\infty}^{+\infty} dl_g e^{-ik_g l_g} \cdot \int_{-\infty}^{+\infty} dl_s e^{-ik_s l_s} U_s(\underline{r}_{\,g}, \underline{r}_{\,s}) \tag{5}$$

where l_g is the distance of the geophone along the geophone line and l_s, the distance of the point source along the source line. $\tilde{G}$ is the Fourier transform of G, and

$$\tilde{G}(k_g, \underline{r}\,) = \frac{i}{2} \frac{exp(i\gamma_g d_g)}{\gamma_g} exp(-ik\hat{g} \cdot \underline{r}\,) \tag{6}$$

$$\tilde{G}(k_s, \underline{r}\,) = \frac{i}{2} \frac{exp(i\gamma_s d_s)}{\gamma_s} exp(-ik\hat{s} \cdot \underline{r}\,) \tag{7}$$

$$\gamma_g = \sqrt{k^2 - k_g^2} \tag{8}$$

$$\gamma_s = \sqrt{k^2 - k_s^2}, \tag{9}$$

where k_g and k_s are the wavenumbers along the geophone line and the source line respectively, γ_g and γ_s are the corresponding perpendicular wavenumbers. $\hat{g}$ and $\hat{s}$ are the unit vectors of plane wave to the geophone line and the source line direction respectively. Substitute Equations (6) and (7) into Equation (4) results in

$$\tilde{U}_s(k_g, k_s) = \frac{k_o^2}{4\gamma_g \gamma_s} exp(i\gamma_g d_g + i\gamma_s d_s) \int_S O(\underline{r}\,) exp[-ik(\hat{g} - \hat{i}) \cdot \underline{r}\,] d\underline{r} \tag{10}$$

where $\hat{i} = -\hat{s}$ is the unit vector in the incident direction. The integration in Equation (10) is in a form of a two dimensional Fourier transform. Therefore it can be written as

$$4\gamma_g\gamma_s\tilde{U}_s(k_g,k_s)exp[-i(\gamma_g d_g+\gamma_s d_s)] = k_o^2\tilde{O}(k(\hat{g}-\hat{i})), \tag{11}$$

where $\tilde{O}(\underline{K})$ is the two dimensional Fourier transform of $O(\underline{r}\ )$. The left hand side of Equation (11) is the plane wave scattering response (or the angular spectrum of the scattered field) which is related to the object spectrum (right hand side).

After measuring the scattered field $U_s(\underline{r}_g, \underline{r}_s)$ and deriving $\tilde{U}_s(k_g,k_s)$ by double Fourier transform, we can obtain the object spectrum from Equation (11). If we have full coverage of the object spectrum $\tilde{O}(\underline{K})$, the object function $O(\underline{r}\ )$ can be obtained by a two dimensional inverse Fourier transform. This is the so called direct Fourier inversion method. In the case of incomplete recovery of $\tilde{O}(\underline{K})$, this method will give distorted image of the object. An alternative of reconstruction is the filtered backpropagation method (Devany 1982, 1984). A comparison of these two approaches is given by Pan and Kak (1983). In the case of incomplete coverage of $\tilde{O}(\underline{K})$, the method of filtered backpropagation, which is used in this paper, is somewhat advantageous. In this approach, the reconstruction operation is applied directly to the angular spectrum of the scattered field $\tilde{U}_s(k_g,k_s)$.

Taking the two dimensional inverse Fourier transform on Equation (11) we get

$$O(\underline{r}\ ) = \frac{1}{(2\pi)^2}\int\int d\underline{K}\tilde{O}(\underline{k})exp[i\underline{K}\cdot\underline{r}\ ]$$

$$= \frac{1}{(2\pi)^2}\int\int dk_s dk_g J(K_x,K_z \mid k_g,k_s)\frac{4\gamma_s\gamma_g}{k_o^2}\tilde{U}_s(k_g,k_s)$$

$$\cdot exp[-i(\gamma_s d_s + \gamma_g d_g)] \cdot exp[i(K_x x + K_z z)], \tag{12}$$

where $J(K_x, K_z \mid k_g, k_s)$ is the Jacobian of coordinate transformation and K_x, K_z are functions of k_g and k_s. Equation (12) is the general reconstruction formula for the given $\tilde{U}_s(k_g, k_s)$. In the following we list the Jacobian, K_x, K_z, and the corresponding reconstruction formulas for different experimental geometries.

a) Vertical Seismic Profiling (VSP)

The VSP geometry is shown in Figure 2(a). Here the source line is at the surface and distance to the source line $d_s = 0$. The distance to geophone line $d_g = x_h$. From this geometry we can obtain

$$K_x = k_s + \gamma_g, \quad K_z = k_g - \gamma_s, \tag{13}$$

and

$$J(K_x, K_z \mid k_s, k_g) = \frac{\partial(K_x, K_z)}{\partial(k_g, k_s)} = \frac{\mid k_g k_s + \gamma_g \gamma_s \mid}{\gamma_g \gamma_s}. \tag{14}$$

Figure 3(a) gives the information coverage in the spectral domain. In the figure, each semi-circle represents the sampled information of the whole receiver line ($-\infty < k_g < +\infty$) for one k_s. We can see that besides some blind areas, where the spectral information of the object can not be detected for this geometry, there are also some areas in which the information is duplicated. For the missing information in the blind areas we will assume it to be zero, that is the strategy of minimum energy inversion (Devany, 1984). However, the information duplication can also be removed to improve the image quality. To do that, we define two windows to remove the high frequency duplication

(the upper ritht part in Figure 3(a)) and the low frequency duplication (the lower left part in Figure 3(a)):

$$W_h(k_g,k_s)=\begin{cases}0 & \text{if } k_g \le -\gamma_s \text{ for } k_s \ge 0\\ 1 & \text{otherwise}\end{cases}$$

$$W_l(k_g,k_s)=\begin{cases}0 & \text{if } k_g \ge \gamma_s \text{ for } k_s \le 0\\ 1 & \text{otherwise}\end{cases}$$

The final reconstruction formula becomes

$$O(x,z)=\frac{2}{\pi}Real\int_{-k_o}^{k_o} dk_s exp(ik_s x - i\gamma_s z)O_1(x,z,k_s), \tag{15}$$

$$O_1(x,z,k_s)=\frac{1}{\pi}\int_{-k_o}^{k_o} dk_g exp[ik_g z - i\gamma_g(x_h - x)]D(k_g,k_s),$$

where

$$D(k_g,k_s)=\tilde{U}_s(k_g,k_s)F(k_g,k_s)$$

$$=\tilde{U}_s(k_g,k_s)W_h(k_g,k_s)W_l(k_g,k_s)\frac{\mid k_g k_s+\gamma_g\gamma_s \mid}{k_o^2} \tag{16}$$

Here $D(k_g,k_s)$ is the filtered angular spectrum of the scattered field and $F(k_g,k_s)$ is the filter function. From Equation (15) we can see that $O_1(x,z,k_s)$ is formed by back-propagating the filtered data $D(k_g,k_s)$ from the geophone line to the object space and $O(x,z)$ is formed by backpropagating $O_1(x,z,k_s)$ to the source line.

b) Surface Reflection Profiling (SRP)

The geometry is shown in Figure 2(b). For this case we have (Wu and Toksöz, 1986)

$$K_x=k_g+k_s, \quad K_z=-(\gamma_g+\gamma_s)$$

$$J(K_x, K_z \mid k_s, k_g) = \frac{\mid k_s\gamma_g - k_g\gamma_s \mid}{\gamma_g\gamma_s} \tag{17}$$

The reconstruction formula Equation (12) now becomes

$$O(x,z) = \frac{1}{\pi} Real \int_{-k_o}^{k_o} dk_s exp[ik_s x - i\gamma_s(z - z_s)] O_1(x,z,k_s), \tag{18}$$

$$O_1(x,z,k_s) = \frac{1}{\pi} \int_{-k_o}^{k_o} dk_g exp[ik_g x - i\gamma_g(z - z_g)] D(k_g, k_s),$$

where

$$D(k_g, k_s) = \tilde{U}_s(k_g, k_s) F(k_g, k_s) = \tilde{U}_s(k_g, k_s) \frac{\mid k_s\gamma_g - k_g\gamma_s \mid}{k_o^2}. \tag{19}$$

Figure 3(b) shows the spectral coverage for this case.

c) Cross-Borehole Transmission (CBT)

The geometry is shown in Figure 2(c). For this case we have

$$K_x = \gamma_g - \gamma_s, \quad K_z = k_g + k_s,$$

$$J(K_x, K_z \mid k_s, k_g) = \frac{\mid k_s\gamma_g + k_g\gamma_s \mid}{\gamma_g\gamma_s} \tag{20}$$

$$d_s = 0, \quad d_g = x_h$$

The reconstruction formulae are (Wu and Toksöz, 1986)

$$O(x,z) = \frac{1}{\pi} Real \int_{-k_o}^{k_o} dk_s exp(ik_s z - i\gamma_s x) O_1(x,z,k_s), \tag{21}$$

$$O_1(x,z,k_s) = \frac{1}{\pi} \int_{-k_o}^{k_o} dk_g exp[ik_g z - i\gamma_g(x_h - x)] D(k_g, k_s),$$

where

$$D(k_g, k_s) = \tilde{U}_s(k_g, k_s) F(k_g, k_s) = \tilde{U}_s(k_g, k_s) \frac{\mid k_s\gamma_g + k_g\gamma_s \mid}{k_o^2}. \tag{22}$$

The spectral coverage for this case is shown in Figure 3(c).

For the case of reconstruction based on the Rytov approximation, all the reconstruction formulas are the same except that $\tilde{U}_s(k_g, k_s)$ is replaced by $\tilde{\Phi}(k_g, k_s)$, which is the double Fourier transform of the complex phase function $\Phi(\underline{r}_g, \underline{r}_s)$ defined by (see Equation (A-22) in Appendix)

$$\Phi(\underline{r}_g, \underline{r}_s) = U_i(\underline{r}_g, \underline{r}_s)\phi_s(\underline{r}_g, \underline{r}_s) \tag{23}$$

where $U_i(\underline{r}_g, \underline{r}_s)$ is the incident field, $\phi_s(\underline{r}_g, \underline{r}_s)$ is the phase of the scattered field.

(II) Multi-source Holography

Multi-source holography is a generalization of the traditional single source holography. This imaging process can be applied to two different classes of objects. One class is the discrete scatterers, such as sharp boundaries, interfaces, edges and corners. Another class is of weak inhomogeneities that satisfy the Born or the Rytov approximations. The latter case has a close relationship to the diffraction tomography (Wu and Toksöz, 1986).

The reconstructed image can be calculated by (Wu and Xu, 1979):

$$I(x,z) = \sum_{m=1}^{M} B_s(\underline{r}_s, \underline{r}) \sum_{n=1}^{N} B_g(\underline{r}, \underline{r}_g) U_{mn}, \tag{24}$$

where $I(x,z)$ is the image strength at the point (x,z) in the object space, U_{mn} is the scattered field measured by the m th receiver for the n th source and

$$B_g(\underline{r}, \underline{r}_g) = exp[-i\frac{w}{C_o}R_g(x,z)],$$

$$B_s(\underline{r}_s, \underline{r}) = exp[-i\frac{w}{C_o}R_s(x,z)].$$

B_g is the backpropagator from the geophone point to the image point; B_s is the backpropagator from the image point to the source point; R_g is the distance between the geophone and the image point; R_s is the distance between the source and the image point. It can be seen that equation (24) is an imaging process by focusing both the receiver array (inner summation) and the source array (outer summation). The direct calculation of equation (24) is time consuming. We use the fast algorithm developed by Wu and Xu (1978) for calculating equation (24), in which the FFT is used.

(III) Algebraic Reconstruction Technique (ART)

Algebraic reconstruction technique (ART) was first introduced by Gordon et al (1970) for three dimensional image reconstruction in electron microscopy and radiology. Due to its adaptability to arbitrary scanning geometries and conceptual simplicity, most geophysical tomography works are based on this type of reconstruction algorithm. Gordon (1974) and Censor (1983) reviewed various modified ART algorithms suitable for various applications. In this study, we use the original ART algorithm, and follow Kak's (1985) formulation. In the ART method, we divide the imaging area into j pixels as shown in Figure 4. Let f_j be the average of a certain physical parameter (such as sonic wave slowness) inside the jth pixel and P_i be the measured line integral or projection of that parameter along the ith ray. Then for an imaging system with N pixels and M

measurements, the relationship between f_j's and P_i's can be written as:

$$\sum_{j=1}^{N} S_{ij} f_j = P_i, \quad i = 1, 2, ...M, \tag{25}$$

where S_{ij} is the length of the segment of the ith ray intersecting the jth pixel. For a given scanning geometry, S_{ij} are specified, so the image reconstruction problem now becomes solving a system of M linear equations for N unknowns. In practice, this system is usually insufficient, inconsistent and too big for direct matrix inversion. So, we use an iterative approach to solve this system of equations. The iterative process is conceptually straightforward. It starts with an initial estimate of the physical parameter inside each pixel in the imaging area. From this initial estimate, the estimated line integral or projection values of the ith ray can be calculated by

$$\hat{P}_i^q = \sum_{j=1}^{N} S_{ij} \hat{f}_j^q \tag{26}$$

where $\hat{f}_j^q$ stands for the estimate of the physical parameter of the jth pixel in the qth iteration and $\hat{P}_i^q$ stands for the estimated projection value of the ith ray in the qth iteration. We then take the difference between the estimated projection value and the measured projection value of the ith ray

$$\triangle P_i^q = P_i - \hat{P}_i^q. \tag{27}$$

From this $\triangle P_i^q$, we can use a "projection method" (such as equation (30)) to find a set of "corrections" $\triangle f_{ij}^q$ that will be applied to each $\hat{f}_j^q$ and bring our estimate $\hat{f}_j^q$ closer to the true solution f_j. By doing this, the ith ray has been used for correction in the qth iteration. The algorithm then continues to examine the $i+1$ th ray, and make corrections on $\hat{f}_j^q$ again. When all the M rays have been examined, one iteration step is

completed. For the next iteration, all the M rays will be examined again and corrections on $\hat{f}_j^q$ will also be made another M times (one time for each ray). This iteration process continues until the sum of the error is smaller than a prespecified threshold and an acceptable estimate of the f_j is obtained.

The most crucial portion of this iteration approach is how to find an appropriate set of corrections $\triangle f_{ij}^q$ that will make this iteration algorithm converge. The "method of projection" proposed by Kaczmarz (1937) is one of those techniques that can solve this problem. M equations in Equation (25) correspond to M hyperplanes in an N-dimensional space. If an unique solution $(f_1, f_2, ...f_N)$ exists, then this solution is a single point in the N-dimensional space. For simplicity, we let M = N = 2 and equation (25) becomes:

$$\begin{aligned} S_{11}f_1 + S_{12}f_2 &= P_1 \\ S_{21}f_1 + S_{22}f_2 &= P_2. \end{aligned} \tag{28}$$

Kaczmarz's projection method is shown in Figure 5. Locating the solution of equation (28) consists of projecting the initial guess on the first hyperplane (in this example, line L_1), reprojecting the projection just obtained onto the second hyperplane (L_2), then projecting back onto the first hyperplane, and so on. If an unique solution exists, the iteration process will always converge to that solution. This projecting process, or equivalently, the method of finding $\triangle \vec{f}_i^q$ in Figure 5 can be written in a vector form:

$$\triangle \vec{f}_i^q = \vec{f}_i^q - \vec{f}_{i-1}^q = \frac{\vec{S}_i(P_i - \vec{f}_{i-1}^q \cdot \vec{S}_i)}{\vec{S}_i \cdot \vec{S}_i}, \tag{29}$$

where $\vec{S}_i = (S_{i1}, S_{i2}, S_{i3}, ...S_{iN})$. We can also write Equation (29) in a form consistent

with Equations (25) to (27):

$$\triangle f_{ij}^q = \frac{S_{ij}(P_i - \sum_{j=1}^N S_{ij}\hat{f}_j^q)}{\sum_{j=1}^N S_{ij}^2} = \frac{S_{ij}(P_i - \hat{P}_i^q)}{\sum_{j=1}^N S_{ij}^2}. \tag{30}$$

We use Equation (30) to calculate $\triangle f_{ij}^q$. There are other approaches (e.g. entropy optimization, quadratic optimization) find $\triangle f_{ij}^q$ and make the iterative algorithm converge. The method used by Dines and Lytle (1979) for cross-borehole tomography is a minimum energy approach. They calculate the $\triangle f_{ij}^q$ by

$$\triangle f_{ij}^q = \frac{(S_{ij})^2(P_i - \hat{P}_i^q)}{\sum_{j=1}^N S_{ij}^2}. \tag{31}$$

Another widely used series expansion method is the simultaneous iterative reconstruction technique (SIRT). The difference between ART and SIRT is how the corrections $\triangle f_{ij}^q$ are applied to each pixel. For ART, each $\hat{f}_j^q$ is updated by $\triangle f_{ij}^q$ everytime when the ith ray is examined and the estimated value for each pixel will be changed M times for one iteration step. For SIRT, $\hat{f}_j^q$ is not changed before all the M rays have been examined, all the $\triangle f_{ij}^q$ have been calculated and put into memory. When all the M rays have been examined, the correction on the jth pixel is the average of all the $\triangle f_{ij}^q$ for $i = 1$ to M. SIRT makes only one correction on each $\hat{f}_j^q$ for one iteration step. The apparent disadvantage of SIRT is it needs more memory than ART. But in some applications, SIRT gives a better reconstruction than ART.

3. ULTRASONIC EXPERIMENTS

Ultrasonic experiments simulating geophysical tomography and multi-source holography are carried out in a modelling tank. This tank is $100cm \times 60cm \times 50cm$ in dimension and is equipped with microcomputer based control and data acquisition systems. Water is used as a constant velocity background medium. Objects of various size and acoustic properties are used as targets to be imaged. We use two broad-band hydrophones as the source (LC-34) and the receiver (ITC-1089D). Frequency range in our experiments is 10 KHz to 200 KHz. Both hydrophones can be moved independently in three dimensional space by three step motors. Each step is equal to 0.064 mm. Translation scanning scheme of hydrophones are controlled by a SLO-SYN step motor controller. Ultrasonic wave is generated at the source hydrophone by a Panametrics 5055PR pulser. The received signals are filtered by a Krohn-Hite 3202R filter, amplified by a Panametrics 5660B preamplifier, and digitized by a Data Precision DATA6000 digital oscilloscope. The digital oscilloscope and the step motor controller are interfaced with the IBM microcomputer by IEEE488 interface bus. Digitized data are transmitted to a VAX 11/780 computer for image reconstruction. Images are displayed on a Comtal image processor. A block diagram of the laboratory set-up is shown in Figure 6.

In the diffraction tomography and ART experiments, we simulate three source-receiver configurations frequently used in geophysical field operations: VSP, cross-borehole, and surface reflection. Figure 3 shows the spatial frequency domain coverage for VSP, cross-borehole, and surface reflection layouts. It should be noticed that these

pictures assume both the source and the receiver are available at infinity. With limited extent of sources and receivers, which is the case in the field and in the laboratory simulation, the area covered by available data in the spatial frequency domain becomes even smaller. The source and receiver configurations used in our experiments are shown in Figure 7.

Object used in the diffraction tomography and the ART experiments is a gelatin cylinder 90 mm in diameter. P-wave velocity and density of this gelatin cylinder are 1.55 Km/sec and 1.24 g/cc respectively. The difference of the P-wave velocity between the object and the background medium is only 4%. This small velocity difference is designed to simulate typical field values and also to satisfy the constraints for using the Born and the Rytov approximations.

In the holography experiments, objects to be imaged is either a single steel bead or a pair of steel cylinders. We choose these objects to demonstrate the applicability of multi-source holography to small and discrete objects. The layout of the holography experiments are shown in Figure 8.

For the diffraction tomography experiments, objects are reconstructed by the filtered backpropagation algorithm (Equation (12)). For the holography experiments, objects are reconstructed using Equation (24). The input to both algorithms are the scattered wavefield induced by the object. Since the scattered wavefield is very weak compared with the incident wavefield, we use a dual-experiment method to measure the scattered wavefield. First, we put the object inside the water tank, scan the source and the

receiver around it, and measure the total wavefield. Then, we remove the object, repeat the same scanning procedure to obtain the incident wavefield. The difference between these two sets of data is the desired scattered wavefield due to the object.

In order to compare the performance of the ART and the filtered backpropagation algorithms, the data collected in the diffraction tomography experiments are also inverted with an ART algorithm. Peak to peak amplitude of the total field waveforms are input to the ART reconstruction algorithm.

4. EXPERIMENTAL RESULTS

(I) Cross-borehole Diffraction Tomography and ART Experiment

The layout of this experiment is shown in Figure 7(a). The source hydrophone is activated at 32 equally spaced positions along a source line, simulating 32 sources in one borehole. The receiver hydrophone records waveforms at 32 equally spaced positions along a receiver line, simulating 32 receivers in another borehole. The gelatin cylinder is placed in the middle of the source line and the receiver line. The ultrasonic wavefield generated at each source position is measured at 32 receiver positions and therefore 32×32 waveforms are recorded for measuring the incident wavefield and the same amount of data are recorded for measuring the total wavefield. The dominant frequency of our signals is 50 KHz. It corresponds to a wavelength of 30 mm in water. The sampling interval between each source or each receiver is 7.62 mm. Waveforms are digitized at a sampling interval of 300 nano-seconds. Figure 9 shows 32 waveforms recorded at 32 receiver positions with the source hydrophone at the middle of the source line. Figure 9(a) shows the total field waveforms, Figure 9(b) the incident field waveforms, and Figure 9(c) the scattered field waveforms. Taking the Fourier transform of the waveforms, we obtain the magnitude and phase of the total field, the incident field, and the scattered field at various frequencies. We use Tribolet's algorithm (Tribolet, 1977) with the computation efficiency improvement made by Bonzanigo (1978) to unwrap the phase data. Using these data, we reconstruct the object with the filtered backpropagation algorithm. Reconstructions with both the Born and the Rytov

approximations are calculated. Figure 10 shows the reconstructions with the Born and Rytov approximations at 30 KHz and 50 KHz. These four images outline the shape and the size of the gelatin cylinder with various fidelity. At the lower frequency, images reconstructed by either the Born or the Rytov approximations are about the same quality (compare Figures 10 (a) and (b)), whereas at higher frequency, image reconstructed by the Rytov approximation is less distorted than that reconstructed by the Born approximation (compare Figures 10 (c) and (d)). This wavelength-independent property of the Rytov approximation observed in this experiment is consistent with the results of the numerical study by Slaney et al (1984). In their work, they demonstrated that the Rytov approximation only requires the phase change per wavelength, not the total phase change. Therefore, as long as the velocity contrast between the object and the surrounding medium is small enough (less than a few percent, as suggested by Slaney et al, 1984), the Rytov approximation is valid without constraints on the size of object. The Born approximation, however, requires the scattered field be small which will be violated when the size of the weak inhomogeneity becomes bigger. It is also noted that in this cross-borehole configuration of sources and receivers, the coverage in the spatial frequency domain is poor in the horizontal direction (see Figure 3(c)), and the resolution in the vertical direction is better than the resolution in the horizontal direction.

The total wavefield measured in the cross-borehole experiment are also used to reconstruct the image of the gelatin cylinder by an ART algorithm. Since the velocity difference between the water and the gelatin cylinder is small, arrival time determination have to be very accurate to give a successful reconstruction. To avoid this difficulty, we

use another physical parameter, the quality factor, to image the gelatin cylinder. Here, peak to peak amplitude of the total field waveforms are input to the ART algorithm. The images reconstructed are shown in Figure 11. Figure 11(a) is the initial guess image. Figure 11(b) is the ART reconstruction after six iterations from Figure 11(a). Figure 11(c) is another initial guess much closer to the true object. Figure 11(d) is the corresponding ART reconstruction after six iterations. Comparing Figures 11 (b) and (d) we note that ART reconstruction improves significantly if the initial model approximates the true object. Further iterations did not improve the images significantly in both cases.

(II) Cross-borehole Experiment With a More Complicate Object

To further investigate the reconstruction algorithms, we run another cross-borehole experiment with a more complicated object. This object is a gelatin cylinder with two aluminum rods inside (see Figure 12). Image reconstructed by the filtered backpropagation algorithm based on the Born approximation is shown in Figure 13(a). Both the gelatin cylinder and the two aluminum rods are successfully reconstructed. The same data are also inverted by the ART. With an initial estimate like Figure 11(a) (assuming no information about the object), the ART reconstruction after six iterations is shown in Figure 13(b). The gelatin cylinder is roughly reconstructed, but the two aluminum rods are missing. This experiment demonstrates that: When the size of the object is comparable with the wavelength, diffraction tomography with the filtered backpropagation reconstruction algorithm can reconstruct this small object better than the ART.

(III) VSP Diffraction Tomography and ART Experiment

In this experiment, the source hydrophone is activated at 32 equally spaced positions along the source line, simulating 32 sources arranged in a straight line on the surface. The receiver hydrophone records waveforms at 32 equally spaced positions along a straight line perpendicular to the source line, simulating 32 receivers in a borehole. Examples of the waveforms recorded are shown in Figure 14. Figure 15 shows the images reconstructed in this experiment with the filtered backpropagation algorithm. Figures 15 (a) (b) (c) (d) are the reconstructions at 30 KHz and 50 KHz with the Born and the Rytov approximations. We noticed that at 50 KHz, reconstructions with the Born approximation has a strong noise at the upper right corner of the imaging area. This noise may due to the interference between two hydrophones. All these four examples reconstruct the upper ritht portion of the object better than the lower left portion. The "bow-tie" shaped artifacts inherent in the VSP migration is stronger in images reconstructed by the Rytov approximation.

Similar to the cross-borehole ART experiment, the peak to peak amplitude of the total field waveforms are used to reconstruct the object by ART. The results of the ART reconstructions are shown in Figure 16. Figure 16 (a) and (c) are initial guess images. Figure 16 (b) and (d) are the corresponding reconstructions after six iterations. Figure 16 shows that with the VSP geometry, ART reconstruction is inferior to the filtered backpropagation reconstruction. The lower left portion of the object, which is not sampled by transmitted rays with the given source-receiver geometry is completely

missed.

(IV) Surface Reflection Diffraction Tomography Experiment

The layout of this experiment is shown in Figure 7(c). The source hydrophone scans along a source line, simulating 32 sources on the surface. The receiver hydrophone scans along another line parallel to the source line, simulating 32 receivers also on the surface. Figure 17 is an example of the waveforms recorded in this surface reflection experiment with the source hydrophone situated at the middle of the source line, where Figure 17(a) is the total field, 17(b) the incident field, and 17(c) is the scattered field. Images reconstructed by the filtered backpropagation algorithm are shown in Figure 18. Figure 18 (a) and (b) are the reconstructions at 30 KHz based on the Born and the Rytov approximations. Figure 18 (c) and (d) are the reconstructions at 50 KHz based on the Born and the Rytov approximations. In this example, the Born approximation performs as well as the Rytov approximation. As discussed by Kaveh et al (1981) and Wu and Aki (1985) the Born approximation performs well for back scattering. In the surface reflection experiment, the dominant forward scattering component which is disturbing for the Born approximation is not received by the receiver. The input to the reconstruction algorithm is the relatively weak back scattering component of the scattered wavefield and this may be the reason why the Born approximation works as well. A common problem of these four reconstructions is that the resolving power in the vertical direction is weaker than the resolving power in the horizontal direction. This phenomenon is consistent with the poor information coverage in the vertical direction

in the spatial frequency domain (Figure 3(b)).

(V) Multi-source Holography Experiment

Two multi-source holography experiments are presented in this paper: a single-source VSP experiment and a multi-source surface reflection experiment. The layout of the VSP experiment is shown in Figure 8(a). In this experiment, the source hydrophone is fixed at one point on the source line. The receiver hydrophone records the wavefield at 64 equally spaced positions along the receiver line. The object is a steel bead with P-wave velocity 5.9 Km/sec and density 7.85 g/cc. Scattered wavefield along the receiver line is obtained by taking the Fourier transform of the 64 scattered field waveforms. By backpropagating the scattered wavefield with Equation (24), we reconstruct the steel bead as shown in Figure 19. Figure 19(a) is reconstructed from the magnitude and phase of the single frequency data at 30 KHz. Figure 19(b) is reconstructed from data at 10 different frequencies ranging from 25 KHz to 34 KHz. In Figure 19(b), interference of the backpropagated wavefield at different frequencies reduces the background noise and the resolution in the horizontal direction is significantly improved. Interfering back-propagated waves at different frequencies is a very straightforward approach of using multi-frequency data. More elaborate approaches of using multi-frequency data such as interpolation in the spatial frequency domain should improve the reconstruction. The layout of the surface reflection experiment is shown in Figure 8(b). In this experiment, the source hydrophone is activated at 5 equally spaced positions along the source line. The receiver hydrophone records the wavefield at 32 equally spaced positions along the

receiver line. Object used in this experiment is a pair of steel cylinders. Holographic reconstructions in this experiment are shown in Figure 20. Figure 20(a) is a single frequency reconstruction at 37 KHz. Figure 20(b) is reconstructed using data at 3 different frequencies from 37 KHz to 44 KHz altogether. Improvement in the resolving power in the vertical direction is obvious. The sides of the objects facing the source line and the receiver line is better reconstructed than the other side of the object.

5. CONCLUSIONS

Both the ART and the diffraction tomography methods can be used for a tomographic imaging of the subsurface structures. These two methods have different adaptability for the available source-receiver configurations and the size and properties of the object. When the source-receiver configuration is such that the insonifying waves are directly transmitted only through part of the object such as the VSP and the surface reflection experiments, the diffraction tomography is superior to the ART. If the object is uniformly illuminated, as is the case of some cross-borehole experiment, the size and the properties of the object determine the best reconstruction algorithm. In the cross-borehole configuration, if the size of the object is comparable to the wavelength, the diffraction tomography method is better than the ART. If the size of the object is much bigger than the wavelength whereas the inhomogeneity is very weak, diffraction tomography may perform as well as ART. If the size of the object is much bigger than the wavelength and the inhomogeneity is strong, curved ray ART will do better than the diffraction tomography. It should be made clear that these conclusions are based on our laboratory set-up where we can separate the scattered wavefield by measuring the background field. In field applications, this arrangement may be possible in enhanced recovery process, fracturing or other cases where "before' and "after" imaging can be made.

Two factors closely related to the fidelity of the geophysical diffraction tomography are also examined in this paper: (1) source-receiver configuration, and (2) approximation

methods. Among the three source-receiver configurations we tested in this study, cross-borehole configuration gives the best result. Images reconstructed with the surface reflection configuration have poor resolution in the vertical direction. VSP configuration images the quadrant of the object facing the source line and the receiver line better than the opposite quadrant of the object.

The Born and the Rytov approximations are also compared based on our experimental data. In this paper, we only reconstructed images with data whose wavelength are $\frac{1}{3}$ (50 KHz examples) or $\frac{1}{1.8}$ (30 KHz examples) of the diameter of the object (gelatin cylinder). This makes it difficult for us to resolve the issue: when the size of the weak inhomogeneity is much bigger than the wavelength, whether the first Rytov approximation is superior to the first Born approximation or not (Chernov, 1960; Kaveh et al, 1981; Slaney et al, 1984; Zapalowski et al, 1985). Our experimental results suggest that the Rytov approximation has a wider range of validity than the Born approximation for the cross-borehole experiment. This is expected since Rytov is better suited to transmission (forward scattering) than Born. For the VSP and the surface reflection experiments, there is no substantial difference between the fidelity of the images reconstructed based on the Born or the Rytov approximations. Our results, however, can at least verify that when the size of the weak inhomogeneity is comparable to the wavelength, the performance of the Born and the Rytov approximation are about the same.

Multi-source holography has the advantage of using arbitrary numbers of sources and receivers at unequally spaced sampling positions. This method does not provide an

accurate value of object properites. For small and discrete objects, however, this study shows that multi-frequency holography can reconstruct the shape of the object.

REFERENCES

Bishop, T. N., Bube, K. P., Cutler, R. T., Langan, R. T., Love, P. L., Resnick, J. R., Shuey, R. T., Spindler, D. A., and Wyld, H. W., 1985, Tomographic determination of velocity and depth in laterally varying media: Geophysics, 50, 903-923.

Bonzanigo, F., 1978, An improvement of Tribolet's phase unwrapping algorithm: IEEE trans., ASSP-26, 104-105.

Censor, Y., 1983, Finite series-expansion reconstruction methods: Proc. IEEE, 71, 409-419.

Chernov, L. A., 1960, Wave propagation in a random medium: McGraw Hill, New York.

Chiu, S. K., Kanasewich, E. R., and Phadke, S., 1986, Three-dimensional determination of structure and velocity by seismic tomography: Geophysics, 51, 1559-1571.

Cottin, J. F., Deletie, P., Francillon, H. J., Lakshmanan, J., Lemoine, Y., and Sanchez, M., 1986, Curved ray seismic tomography: application to the Grand Dam (Reunion Island): First Break, 4, 25-30.

Devany, A. J., 1982, A filtered back propagation algorithm for diffraction tomography: Ultrasonic Imag., 4, 336-350.

Devany, A. J., 1984, Geophysical diffraction tomography: IEEE trans., GE-22, 3-13.

Dines, K. A., and Lytle, R. J., 1979, Computerized geophysical tomography: Proc. IEEE,

67, 1065-1073.

Esmersoy, C., 1986, The backpropagated field approach to multidimensional velocity inversion: Ph. D. thesis, Massachusetts Institute of Technology.

Gordon, R., Bender, R., and Herman, G. T., 1970, Algebraic reconstruction techniques (ART) for three-dimensional electron microscopy and X-ray photography: J. Theor. Biol., 29, 471-481.

Gordon, R., and Herman, G. T., 1974, Three-dimensional reconstruction from projections: a review of algorithms: Int. Rev. Cytol., 38, 111-151.

Gustavsson, M., Ivansson, S., Moren, P., and Pihl, J., 1986, Seismic borehole tomography — measurement system and field studies: Proc. IEEE, 74, 339-346.

Ivansson, S., 1985, A study of methods for tomographic velocity estimation in the presence of low-velocity zones: Geophysics, 50, 969-988.

Ivansson, S., 1986, Seismic borehole tomography — theory and computational methods: Proc. IEEE, 74, 328-338.

Kaczmarz, S., 1937, Angenaherte auflosung von systemen linearer gleichungen: Bull. Acad. Pol. Sci. Lett., A, 355-357.

Kak, A. C., 1985, Tomographic imaging with diffracting and non-diffracting sources: Array Signal Processing, Haykin, S., ed., Englewood Cliffs, New Jersey, Prentice Hall.

Kaveh, M., Soumekh, M., and Muller, R. K., 1981, A comparison of Born and Rytov approximation in acoustic tomography: Acoustical Imaging, 11, Powers, J. P., ed., Plenum Press, New York, 325-335.

Kretzschmar, J. L. and Witterholt, E. J., 1984, Enhanced recovery surveillance using well-to-well tomography: SPE/DOE -12680.

Lewitt, R. M., 1983, Reconstruction algorithms: transform methods: Proc. IEEE, 71, 390-408.

McMechan, G. A., 1983, Seismic tomography in boreholes: Geophys. J. R. astr. Soc., 74, 601-612.

Menke, W., 1984, The resolving power of cross-borehole tomography: Geophys. Res. Lett., 11, 105-108.

Mersereau, R. M. and Oppenheim, A. V., 1974, Digital reconstruction of multi-dimensional signals from their projections: Proc. IEEE, 62, 1319-1338.

Mueller, R. K., Kaveh, M., and Wade, G., 1979, Reconstructive tomography and applications to ultrasonics: Proc. IEEE, 67, 567-587.

Mueller, R. K., Kaveh, M., and Inverson, R. D., 1980, A new approach to acoustic tomography using diffraction techniques: Acoustical Imaging, 8, Metherell, A. F., ed., Plenum Press, New York, 615-628.

Pan, S. X. and Kak, A. C., 1983, A computational study of reconstruction algorithms for

diffraction tomography: interpolation versus filtered backpropagation: IEEE trans., ASSP-31, 1262-1275.

Peterson, J. E., Paulsson, B. N. P., and McEvilly, T. V., 1985, Applications of algebraic reconstruction techniques to crosshole seismic data: Geophysics, 50, 1566-1580.

Ramirez, A. L., 1986, Recent experiments using geophysical tomography in fractured granite: Proc. IEEE, 74, 347-452.

Slaney, M., Kak, A. C., and Larsen, L., 1984, Limitations of imaging with first-order diffraction tomography: IEEE trans., MTT-32, 860-874.

Tribolet, J. M., 1977, A new phase unwrapping algorithm: IEEE trans., ASSP-25, 170-177.

Wu, R. S. and Aki, K., 1985, Scattering characteristics of elastic waves by an elastic heterogeneity: Geophysics, 50, 582-595.

Wu, R. S. and Toksöz, M. N., 1986, Diffraction tomography and multi- source holography applied to seismic imaging: Geophysics, in press.

Wu, R. S. and Xu, S. H., 1978, A fast algorithm for near region in holographic reconstruction: Acta Geophysica Sinica, 21, 262-267.

Wu, R. S. and Xu, S. H., 1979, Digital holography applied to borehole electromagnetic wave exploration: Acta Seismologica Sinica, 1, 197-213.

Zapalowski, L., Leeman, S., and Fiddy, M. A., 1985, Image reconstruction fidelity using the Born and Rytov approximations: Acoustical Imaging, 14, Berkhout, A. J., Ridder, J., and van der Wal, L. F., eds., Plenum Press, New York, 295-304.

APPENDIX A. DERIVATION OF THE LIPMANN-SCHWINGER EQUATION BASED ON THE FIRST BORN AND FIRST RYTOV APPROXIMATION

Equation (1) in section 2 is the Lippmann-Schwinger equation and is the starting point of the derivation of our filtered backpropagation reconstruction algorithm. It is a linearized solution to the wave equation. This linearization is based on the first Born approximation. In this Appendix, we will derive Equation (1) and show how we use the Born approximation in our derivation. Besides the Born approximation, our reconstruction algorithm can also be based on the first Rytov approximation. In the second half of this appendix, we will find a solution to the wave equation with another approach and linearize this solution by the Rytov approximation. This linearized solution is therefore the Rytov approximation counterpart of Equation (1). Comparing this solution with Equation (1), we will notice that these two solutions are very similar. The only difference in the reconstruction algorithms with the Born or the Rytov approximation is that when we use the Born approximation, input to the reconstruction algorithm is the scattered wavefield, whereas when we use the Rytov approximation, input to the reconstruction algorithm is the complex phase function defined by Equation (23) in section 2.

The First Born Approximation

To derive Equation (1), we start with the acoustic wave equation in an inhomogeneous medium

$$(\nabla^2 + K^2(\underline{r}\,))U_t(\underline{r}\,) = 0. \tag{A-1}$$

$U_t(\underline{r}\,)$ is the total wavefield and is assumed to be the sum of the incident field $U_i(\underline{r}\,)$ and the scattered field $U_s(\underline{r}\,)$.

$$U_t(\underline{r}\,) = U_i(\underline{r}\,) + U_s(\underline{r}\,). \tag{A-2}$$

With the definition of the object function in section 2, we can write

$$K^2(\underline{r}\,) = k_o^2 - k_o^2 O(\underline{r}\,), \tag{A-3}$$

k_o is the wavenumber of the homogeneous background medium. Substitute Equation (A-2) and (A-3) into Equation (A-1), we have:

$$(\nabla^2 + k_o^2)[U_i(\underline{r}\,) + U_s(\underline{r}\,)] = k_o^2 O(\underline{r}\,)[U_i(\underline{r}\,) + U_s(\underline{r}\,)]. \tag{A-4}$$

Since $(\nabla^2 + k_o^2)U_i(\underline{r}\,) = 0$, Equation (4) becomes:

$$(\nabla^2 + k_o^2)U_s(\underline{r}\,) = k_o^2[U_i(\underline{r}\,) + U_s(\underline{r}\,)]. \tag{A-5}$$

The solution to Equation (A-5) can be expressed as an integral equation:

$$U_s(\underline{r}\,) = -k_o^2 \int O(\underline{r}\,\prime)[U_i(\underline{r}\,\prime) + U_s(\underline{r}\,\prime)]G(\underline{r}\,, \underline{r}\,\prime)d\underline{r}\,\prime \tag{A-6}$$

where $G(\underline{r}\,, \underline{r}\,\prime)$ is the free space Green's function. It is noticed that Equation (A-6) is a nonlinear relationship between $U_s(\underline{r}\,)$ and $O(\underline{r}\,)$. To derive a feasible reconstruction

algorithm, we need a linear relationship between $U_s(\underline{r}\,)$ and $O(\underline{r}\,)$. As long as the inhomogeneity in our experiment is very weak so that $U_s(\underline{r}\,) \ll U_i(\underline{r}\,)$, we can use the first Born approximation to achieve this linearity. Using the first Born approximation, we set $U_s(\underline{r}\,) = 0$ inside the integral of Equation (A-6) and Equation (A-6) becomes:

$$U_s(\underline{r}\,) = -k_o^2 \int O(\underline{r}\,\prime) U_i(\underline{r}\,\prime) G(\underline{r}\,, \underline{r}\,\prime) d\underline{r}\,\prime. \tag{A-7}$$

For a point source, the incident field $U_i(\underline{r}\,)$ can be replaced by a Green's function and Equation (A-7) can be written as

$$U_s(\underline{r}_{\,g}, \underline{r}_{\,s}) = -k_o^2 \int O(\underline{r}\,) G(\underline{r}\,, \underline{r}_{\,s}) G(\underline{r}\,, \underline{r}_{\,g}) d\underline{r}\,. \tag{A-8}$$

$U_s(\underline{r}_{\,g}, \underline{r}_{\,s})$ is the scattered wavefield measured at $\underline{r}_{\,g}$ when the point source is located at $\underline{r}_{\,s}$. Equation (A-8) is identical to Equation (1) in section 2. It relates the measured data $U_s(\underline{r}_{\,g}, \underline{r}_{\,s})$ with the object function $O(\underline{r}\,)$ linearily and therefore is the starting point in the derivation of our reconstruction algorithm.

The First Rytov Approximation

In this section, we use another method to solve the wave equation. Let the total wavefield be represented as:

$$U_t(\underline{r}\,) = exp[\phi_t(\underline{r}\,)], \tag{A-9}$$

where $\phi_t(\underline{r}\,)$ is the phase of the total wavefield. Substitute Equation (A-9) into Equation (A-1), Equation (A-1) becomes:

$$\nabla^2 \phi_t(\underline{r}\,) + [\nabla \phi_t(\underline{r}\,) \cdot \nabla \phi_t(\underline{r}\,)] + K^2(\underline{r}\,) = 0. \tag{A-10}$$

Use the relationship between $K(\underline{r})$ and $O(\underline{r})$ in Equation (A-3), and omit $\underline{r}$ in $\phi_t(\underline{r})$ and $K(\underline{r})$ for simplicity, Equation (A-10) can be written as:

$$\nabla^2\phi_t + (\nabla\phi_t \cdot \nabla\phi_t) + k_o^2 = k_o^2 O(\underline{r}) \tag{A-11}$$

We assume that

$$\phi_t = \phi_i + \phi_s. \tag{A-12}$$

Where ϕ_i is the phase of the incident wavefield and ϕ_s is the phase of the scattered wavefield. Substitute Equation (A-12) into Equation (A-11), we obtain

$$[\nabla^2\phi_i + \nabla\phi_i \cdot \nabla\phi_i + k_o^2] + 2(\nabla\phi_i \cdot \nabla\phi_s) + \nabla^2\phi_s = -(\nabla\phi_s \cdot \nabla\phi_s) + k_o^2 O(\underline{r}). \tag{A-13}$$

Since those terms inside the square brackets of Equation (A-13) is just another form of the homogeneous wave equation, so

$$\nabla^2\phi_i + \nabla\phi_i \cdot \nabla\phi_i + k_o^2 = 0. \tag{A-14}$$

Equation (A-13) now becomes:

$$2(\nabla\phi_i \cdot \nabla\phi_s) + \nabla^2\phi_s = -(\nabla\phi_s \cdot \nabla\phi_s) + k_o^2 O(\underline{r}) \tag{A-15}$$

We now use the equality relationship

$$\nabla^2(U_i\phi_s) = \phi_s\nabla^2 U_i + 2\nabla U_i \cdot \nabla\phi_s + U_i\nabla^2\phi_s. \tag{A-16}$$

Equation (A-16) can be rearranged as

$$2\nabla U_i \cdot \nabla\phi_s + U_i\nabla^2\phi_s = (\nabla^2 + k_o^2)U_i\phi_s. \tag{A-17}$$

Combine Equation (A-15) and (A-17) gives

$$(\nabla^2 + k_o^2)U_i\phi_s = U_i[-(\nabla\phi_s \cdot \nabla\phi_s) + k_o^2 O(\underline{r})]. \tag{A-18}$$

We can express the solution to Equation (A-18) as an integral equation:

$$U_i(\underline{r}\,)\phi_s(\underline{r}\,) = -\int U_i(\underline{r}\,')[-\nabla\phi_s(\underline{r}\,')\cdot\nabla\phi_s(\underline{r}\,') + k_o^2 O(\underline{r}\,')]G(\underline{r}\,,\underline{r}\,')d\underline{r}\,'. \qquad \text{(A-19)}$$

Equation (A-19) is a nonlinear relationship between the measured data $\phi_s(\underline{r}\,)$ and the object function $O(\underline{r}\,)$. The first Rytov approximation can now be used to linearize Equation (A-19) presumming $\nabla\phi_s(\underline{r}\,)$ is small. For small $\nabla\phi_s(\underline{r}\,)$, the quantity $(\nabla\phi_s(\underline{r}\,)\cdot \nabla\phi_s(\underline{r}\,))$ inside the integral is neglected by the first Rytov approximation and Equation (A-19) becomes:

$$U_i(\underline{r}\,)\phi_s(\underline{r}\,) = -k_o^2\int U_i(\underline{r}\,')O(\underline{r}\,')G(\underline{r}\,,\underline{r}\,')d\underline{r}\,'. \qquad \text{(A-20)}$$

For a point source at $\underline{r}_s$, the incident field at $\underline{r}$ is:

$$U_i(\underline{r}\,) = G(\underline{r}\,,\underline{r}_s). \qquad \text{(A-21)}$$

Equation (A-20) can then be written as:

$$U_i(\underline{r}_g,\underline{r}_s)\phi_s(\underline{r}_g,\underline{r}_s) = -k_o^2\int O(\underline{r}\,)G(\underline{r}\,,\underline{r}_s)G(\underline{r}\,,\underline{r}_g)d\underline{r}\,. \qquad \text{(A-22)}$$

Equation (A-22) is a linear relationship between the measured data $U_i(\underline{r}_g,\underline{r}_s)\phi_s(\underline{r}_g,\underline{r}_s)$ and the object function $O(\underline{r}\,)$. Notice that the right hand side of Equation (A-22) is exactly the same as the right hand side of Equation (A-8). This means that although the filtered backpropagation reconstruction algorithm derived from Equation (A-8) in section 2 is based on the Born approximation, a filtered backpropagation algorithm based on the Rytov approximation is obtained simply by changing the input to the algorithm from $U_s(\underline{r}_g,\underline{r}_s)$ for the Born approximation to $U_i(\underline{r}_g,\underline{r}_s)\phi_s(\underline{r}_g,\underline{r}_s)$ for the Rytov approximation.

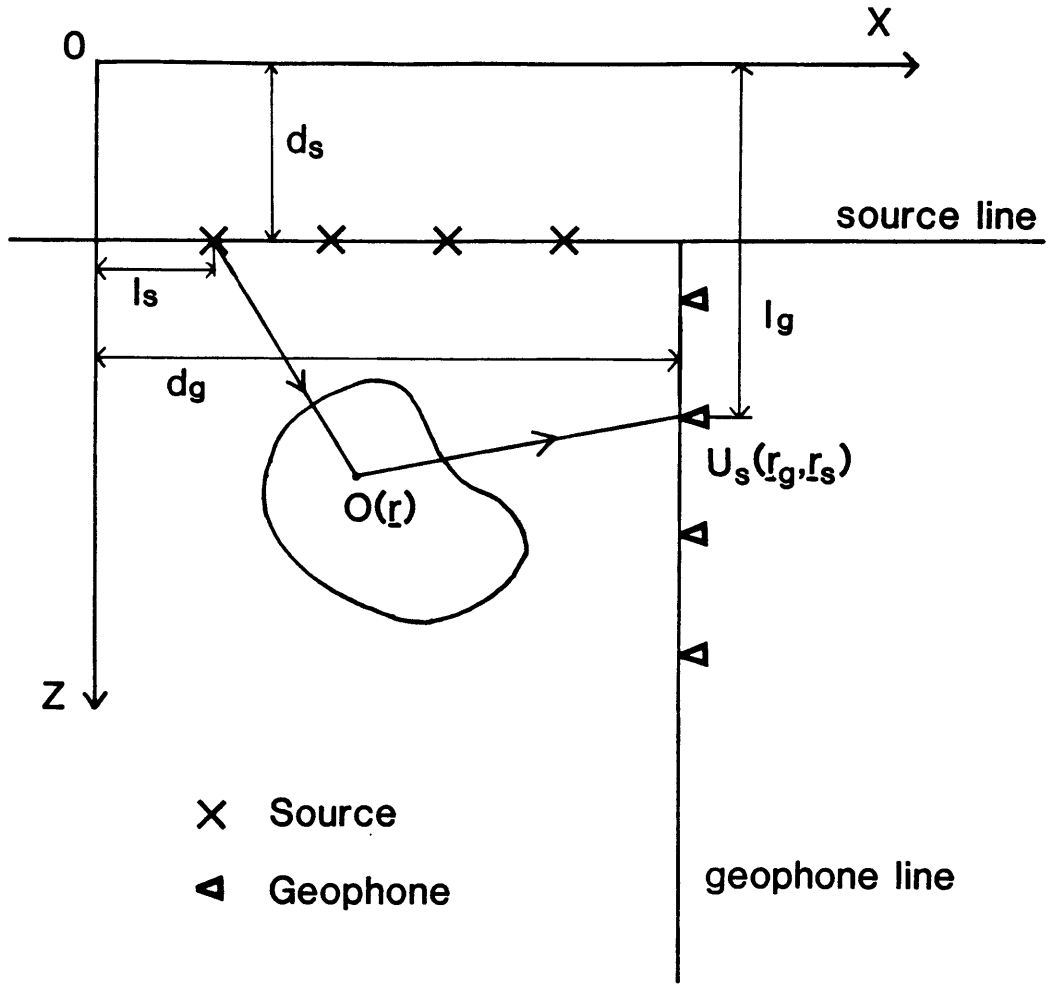

Figure 1: Two-dimensional geometry used in the derivation of the filtered backpropagation algorithm. $O(\underline{r})$ is the object function. $U_s(\underline{r}_g, \underline{r}_s)$ is the measured scattered wavefield. The vertical distance from the origin to the source line and the geophone line are d_s and d_g respectively. l_s is the distance of the source along the source line. l_g is the distance of the geophone along the geophone line.

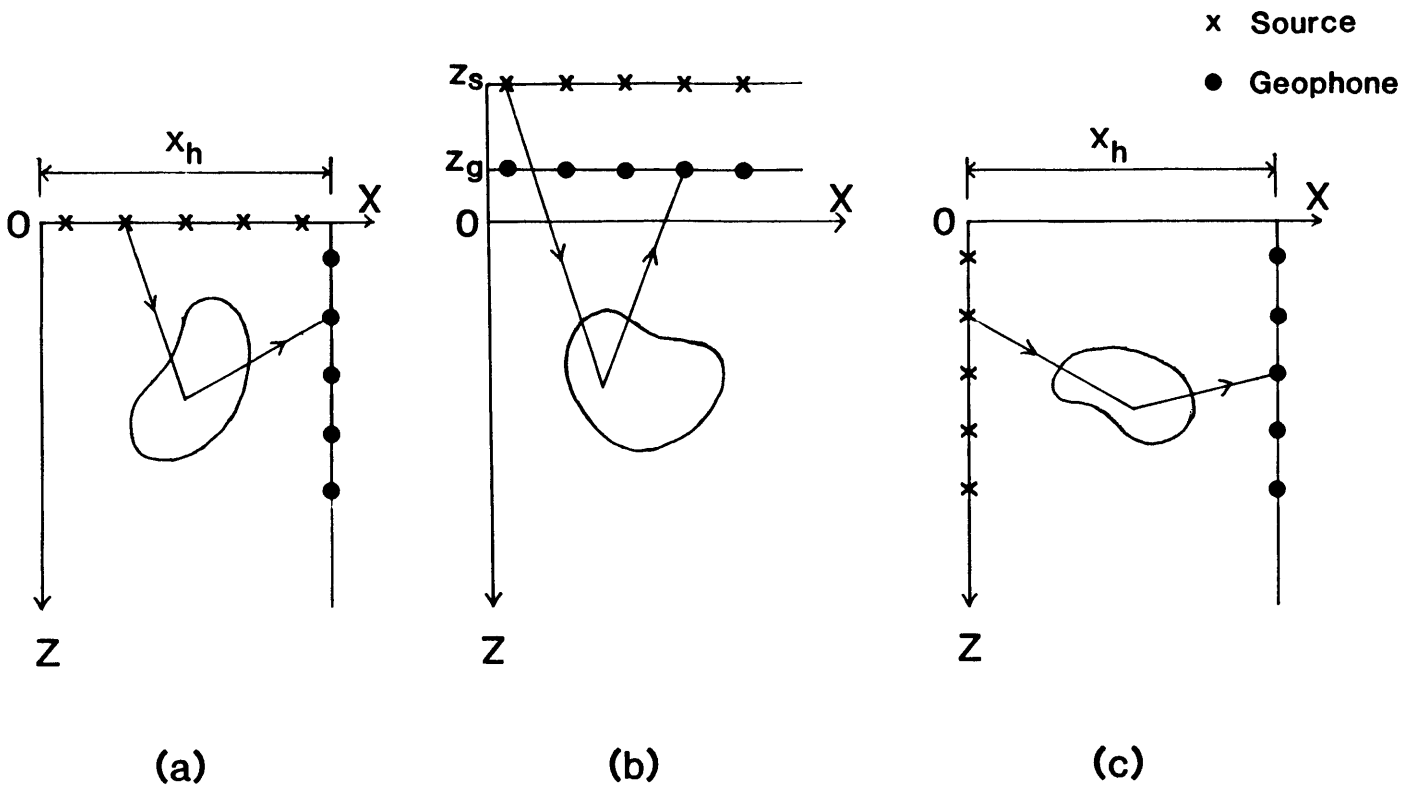

Figure 2: Three source-receiver configurations used in this study. (a) VSP experiment. (b) Surface reflection experiment. (c) Cross-borehole experiment.

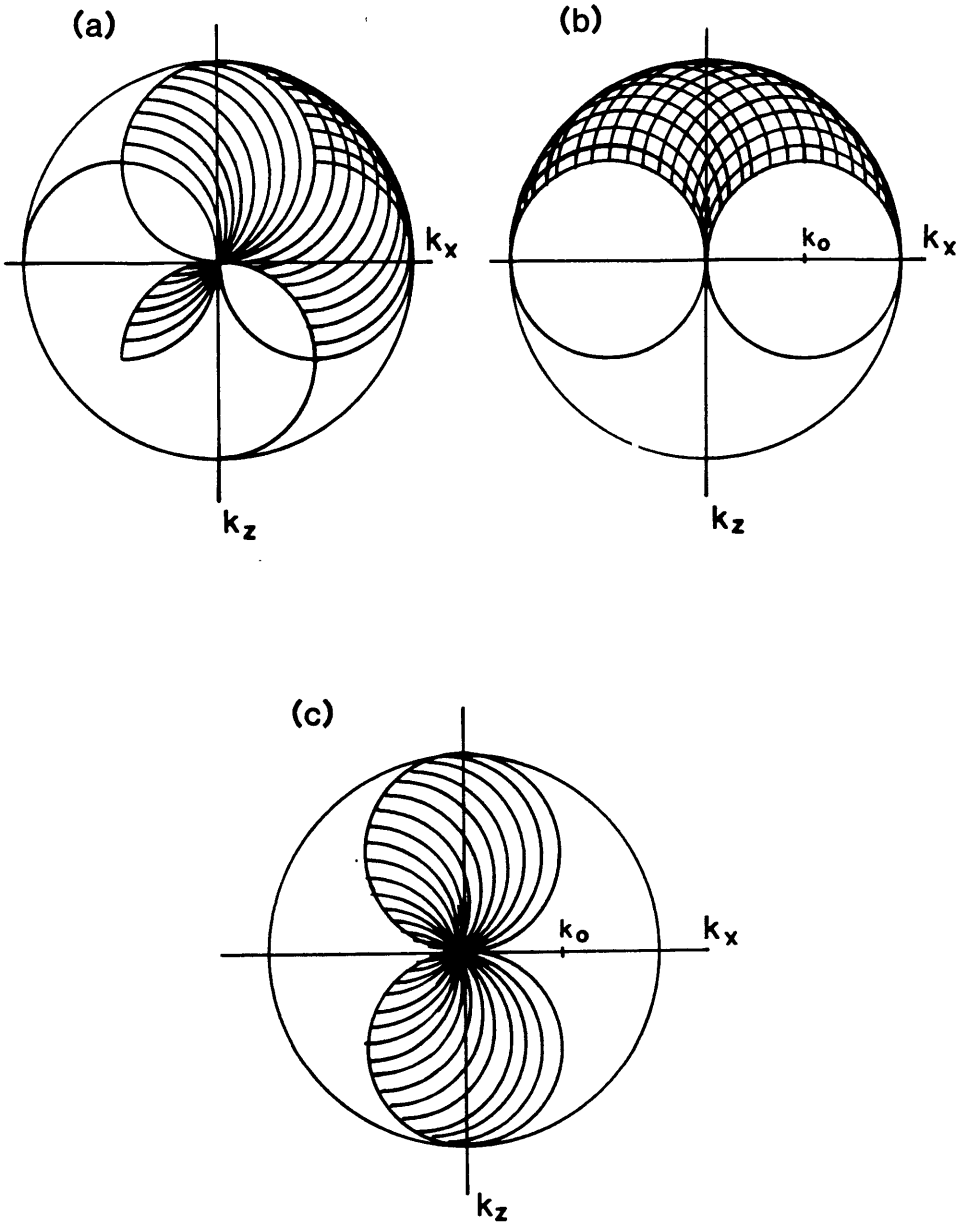

Figure 3: The information coverage in the spatial frequency domain of the three source-receiver configurations used in this study. (a) VSP experiment. (b) Surface reflection experiment. (c) Cross-borehole experiment. k_o is the wavenumber in the constant background medium.

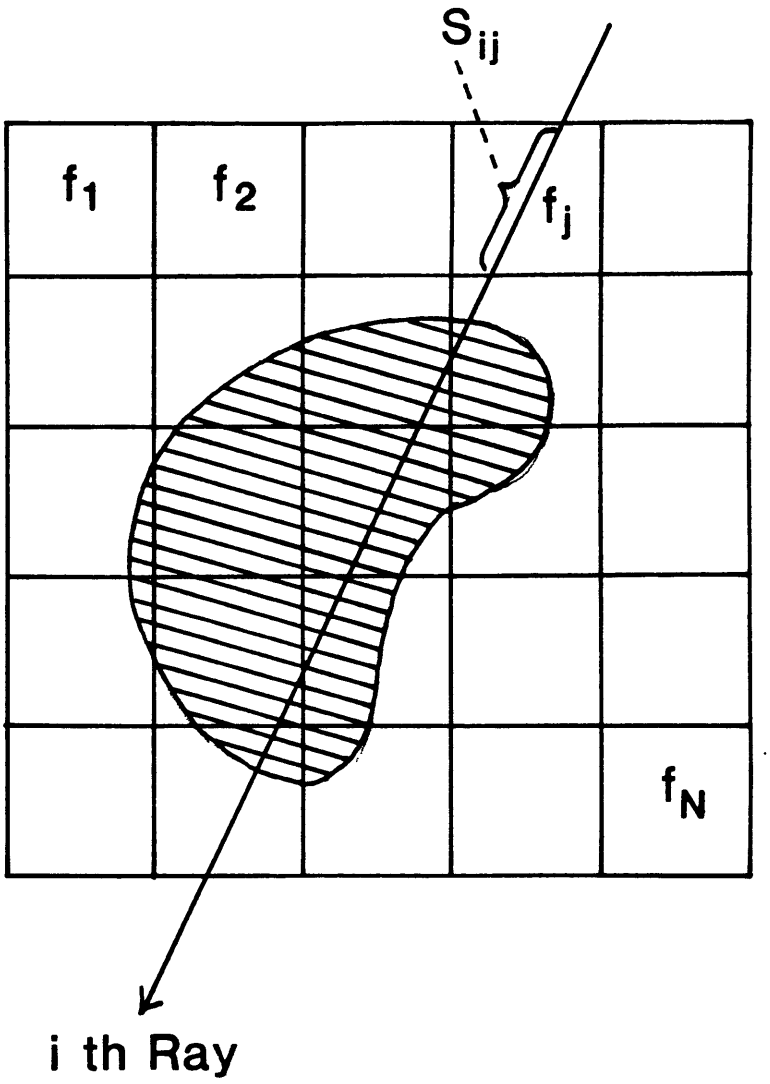

Figure 4: For the ART reconstruction, the imaging area is divided into N pixels. f_j is the average of a certain physical parameter inside the jth pixel. S_{ij} is the length of the segment of the ith ray intersecting the jth pixel.

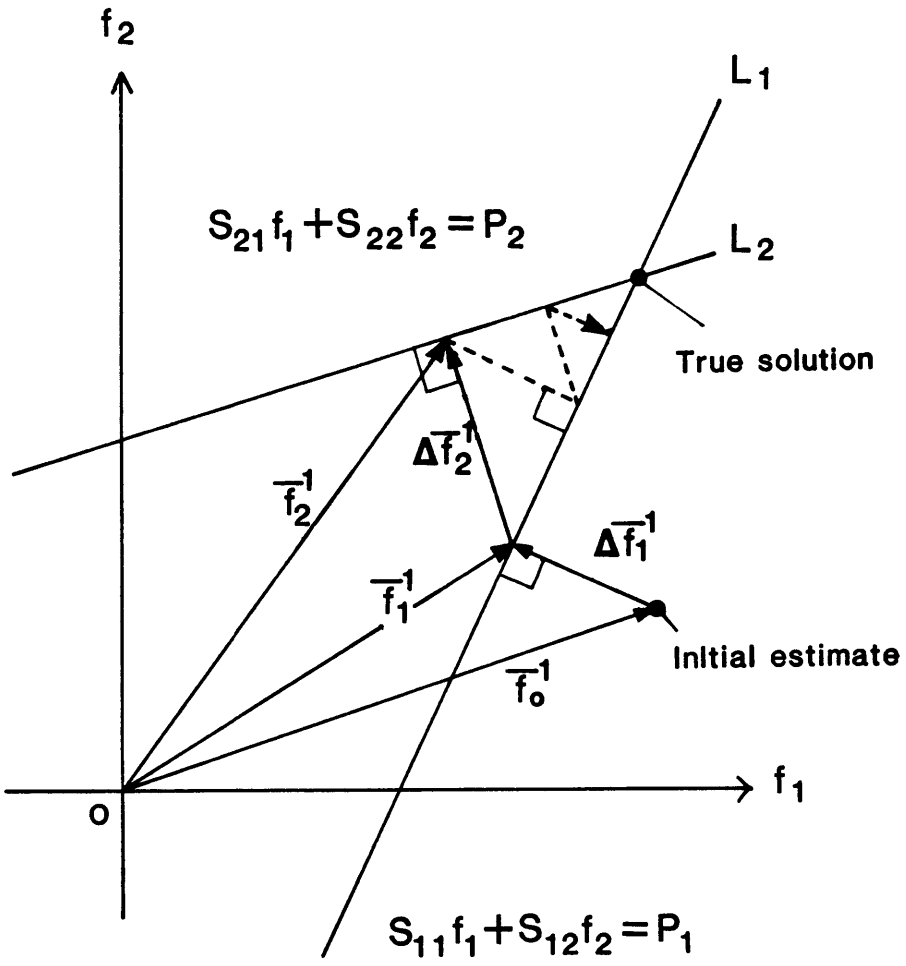

Figure 5: Illustration of Kacmarz's projection method of solving a system of linear equations.

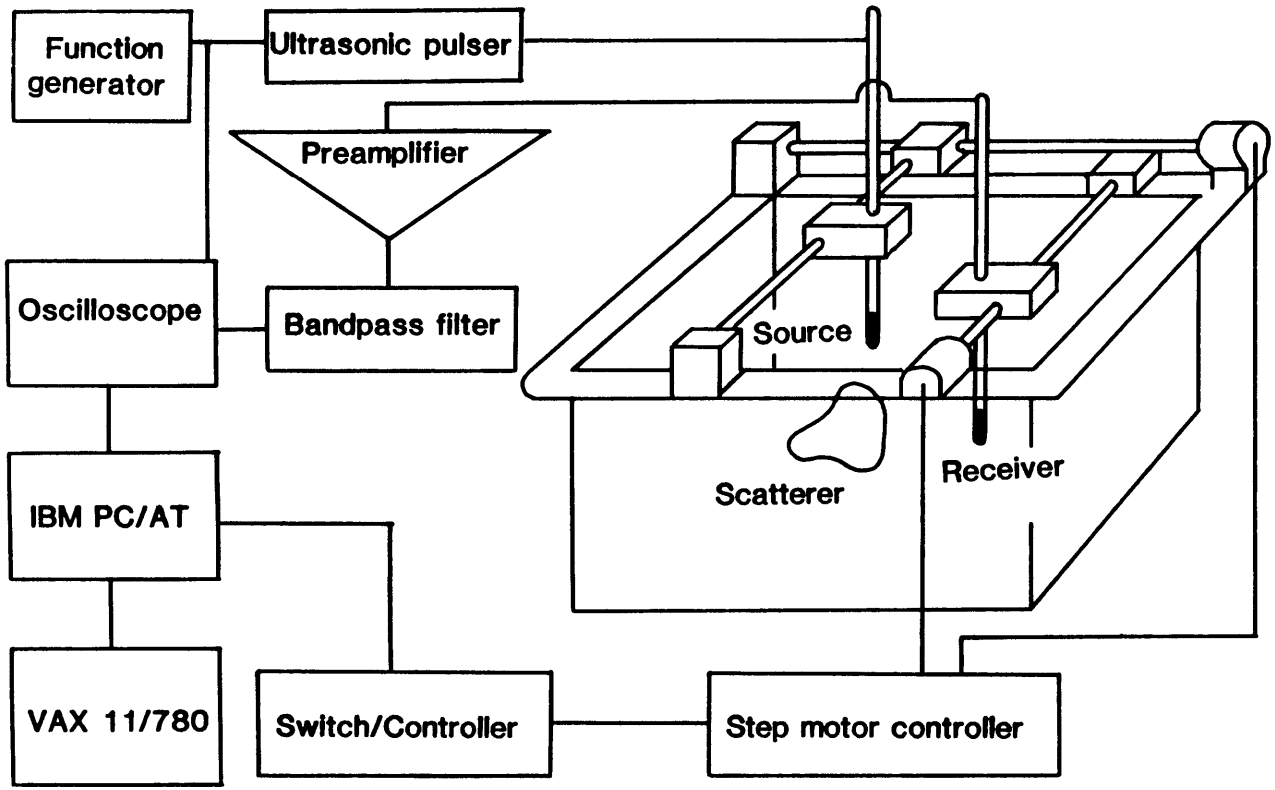

Figure 6: Block diagram of the microcomputer based ultrasonic imaging system.

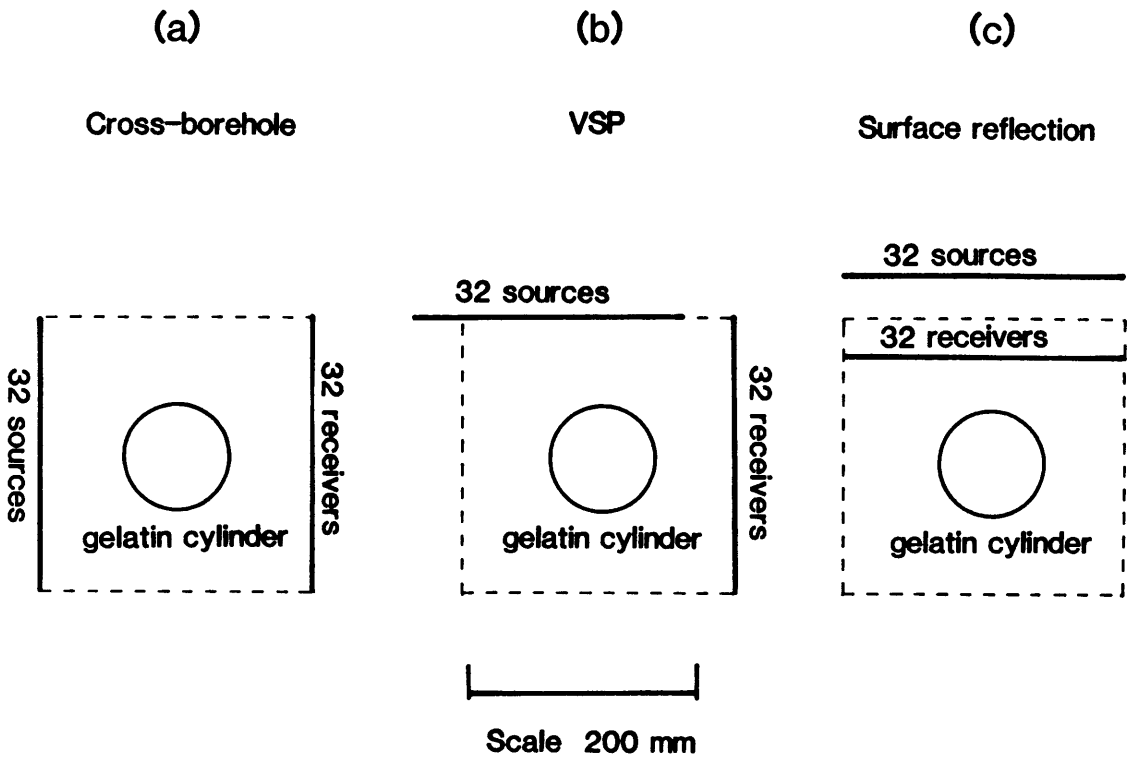

Figure 7: Top view of the actual layout of the tomography experiments. (a) Cross-borehole experiment. (b) VSP experiment. (c) Surface reflection experiment.

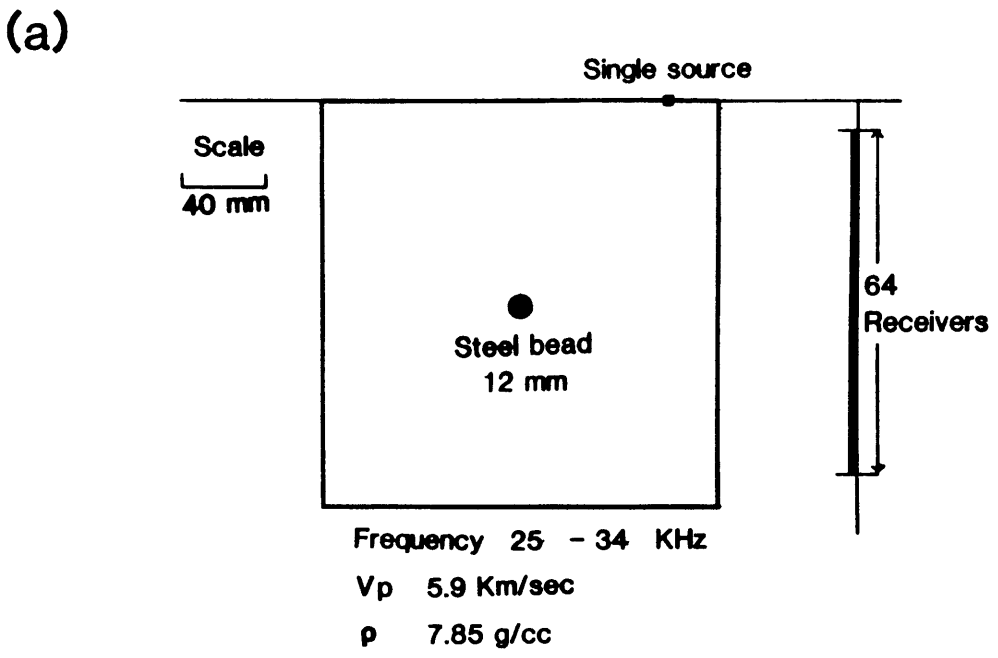

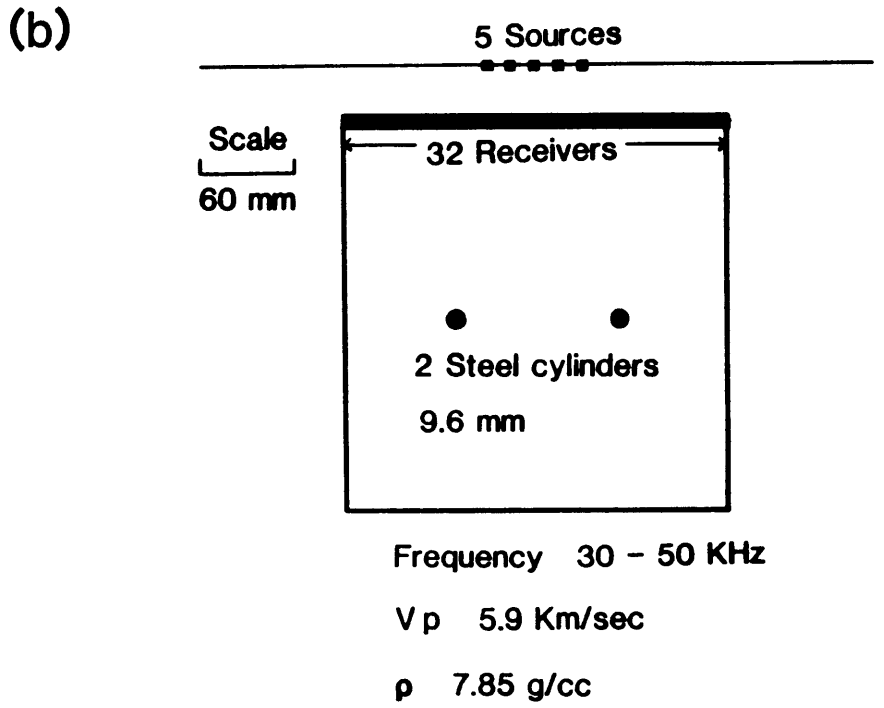

Figure 8: Top view of the layout of the holography experiments. (a) VSP holography experiment. (b) Surface reflection holography experiment.

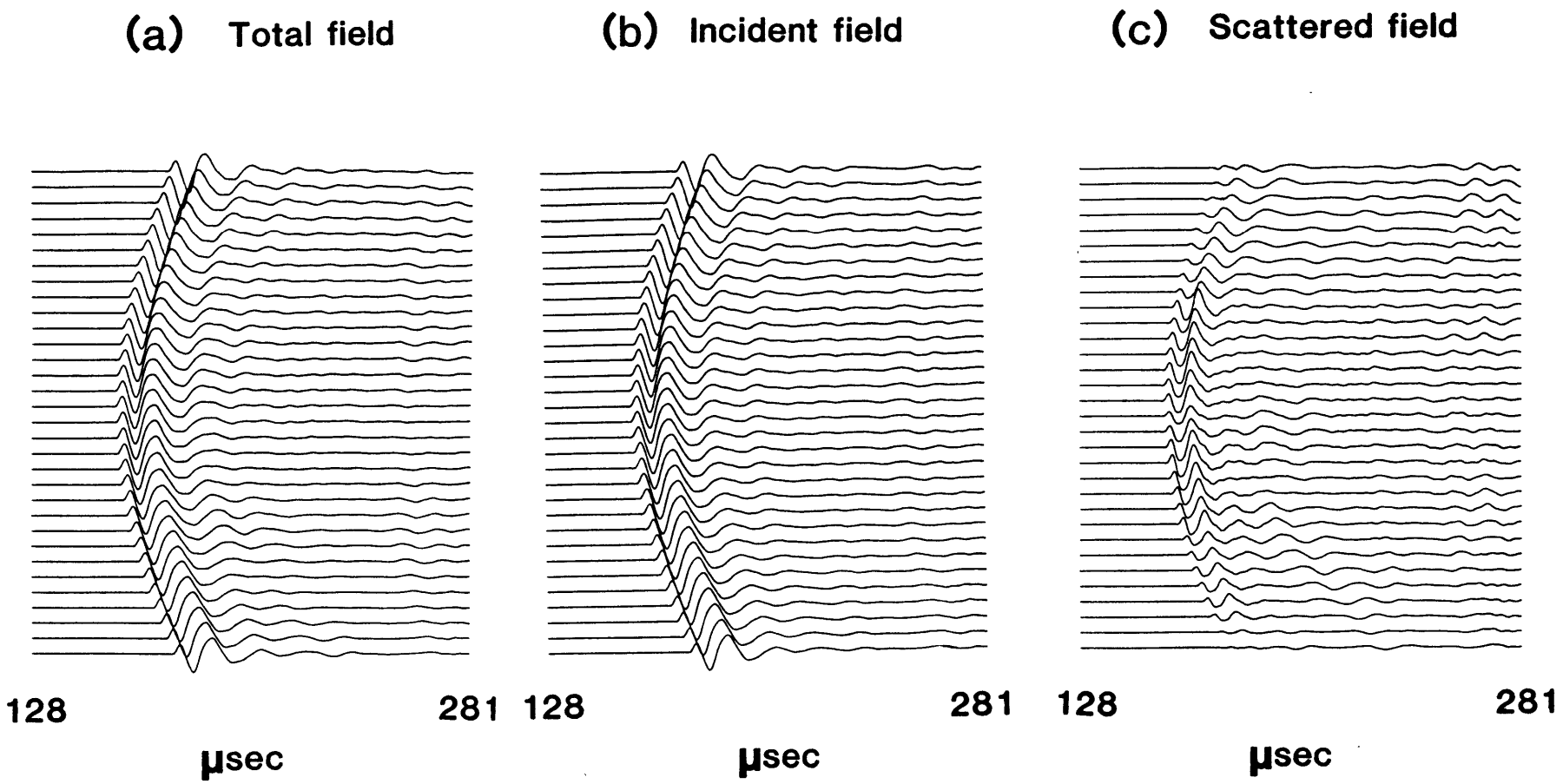

Figure 9: Examples of waveforms recorded in the cross-borehole experiment. (a) Total field waveforms. (b) Incident field waveforms. (c) Scattered field waveforms.

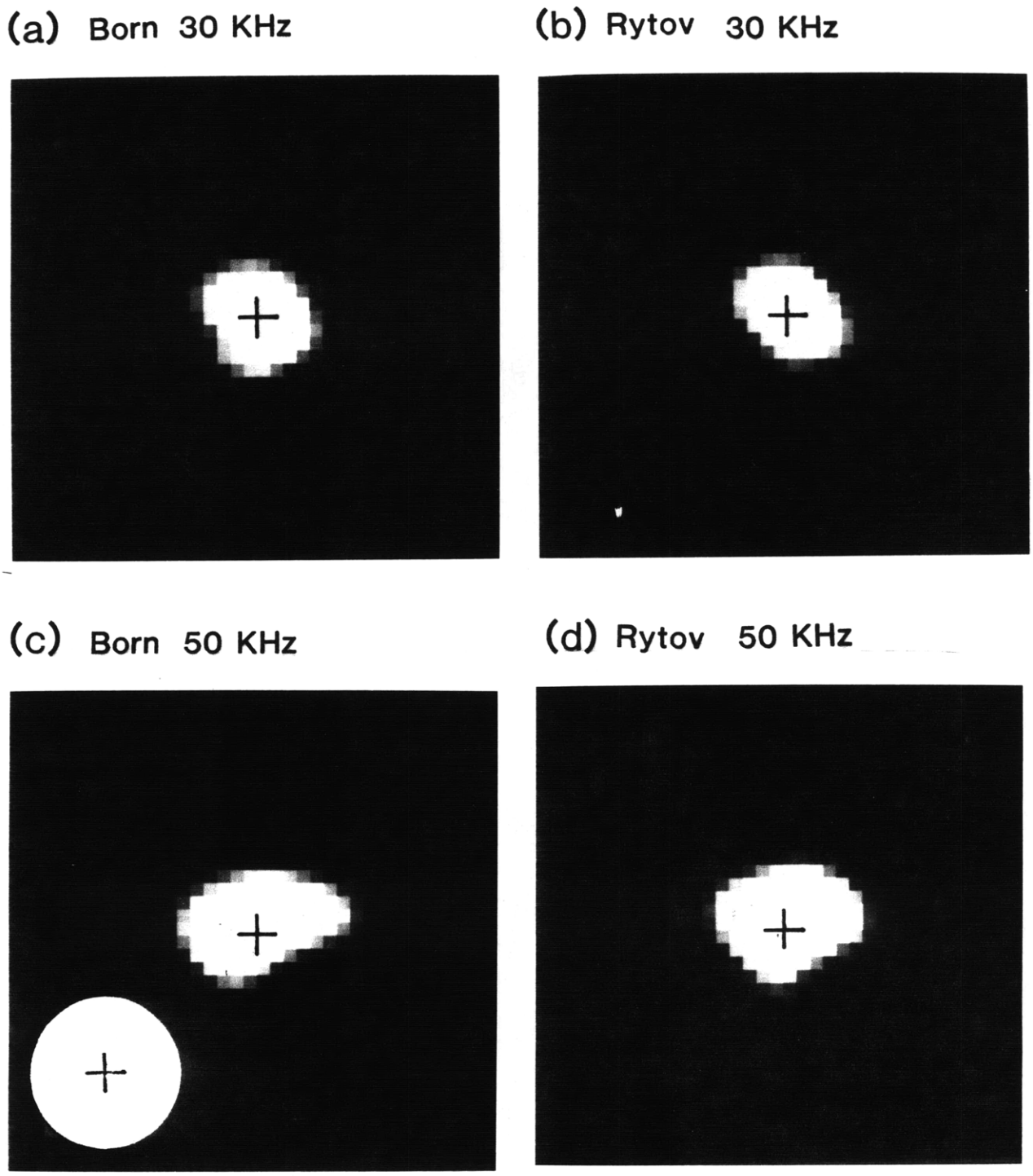

Figure 10: Images reconstructed by the filtered backpropagation algorithm in the cross-borehole experiment. The gelatin cylinder should be centered at the cross with the size and shape as shown by the white circle at the lower left corner of the figure. (a) Reconstruction with the Born approximation at 30 KHz. (b) Reconstruction with the Rytov approximation at 30 KHz. (c) Reconstruction with the Born approximation at 50 KHz. (d) Reconstruction with the Rytov approximation at 50 KHz.

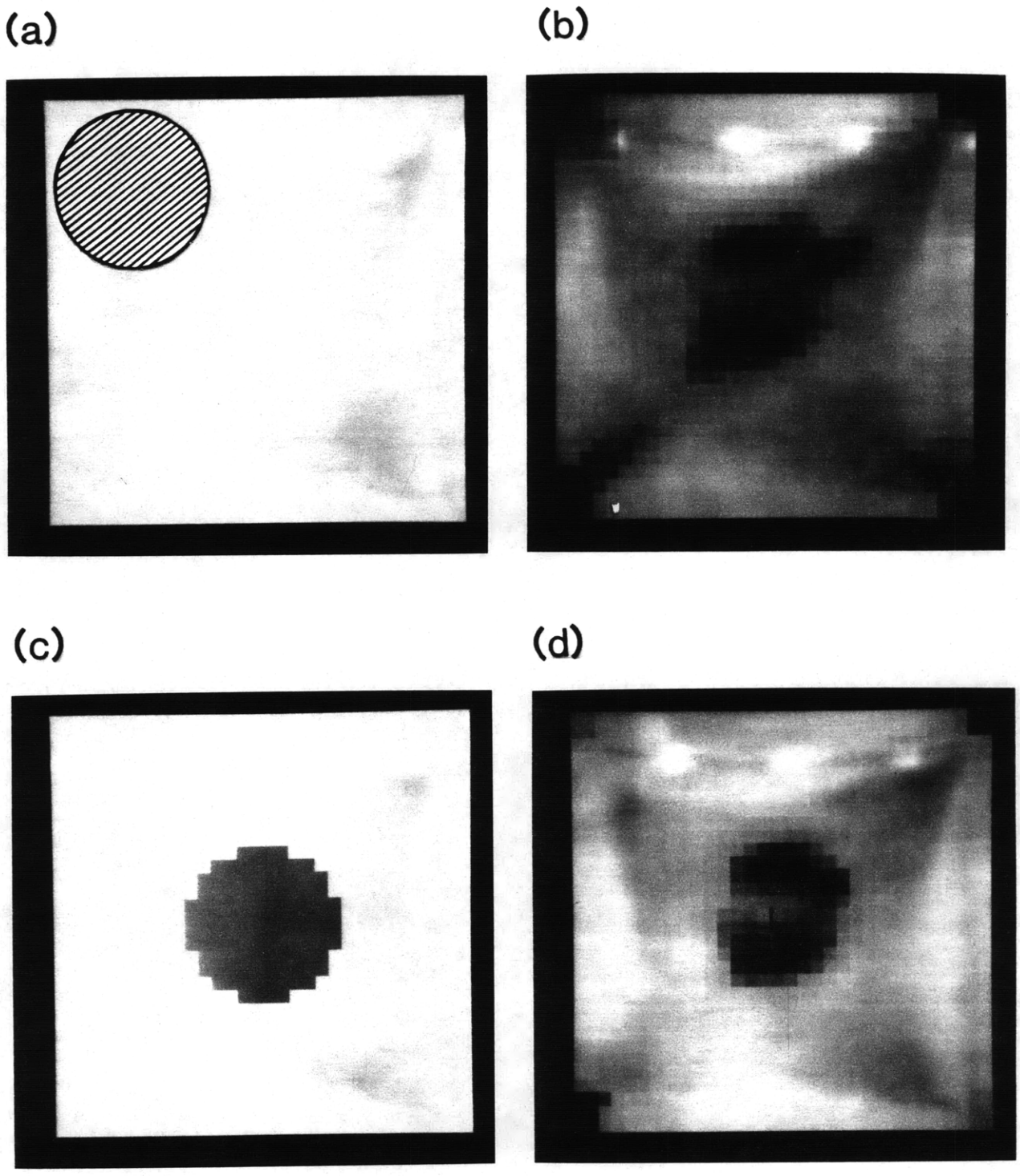

Figure 11: Images reconstructed by the ART algorithm in the cross-borehole experiment. The gelatin cylinder should be centered at the cross with the size and shape as shown by the shaded circle at the upper left corner of the figure. (a) An initial estimate assuming no information about the object function. (b) ART reconstruction with an initial estimate like (a) after six iterations. (c) An initial estimate very close to the true object function. (d) ART reconstruction with an initial estimate such as (c) after six iterations.

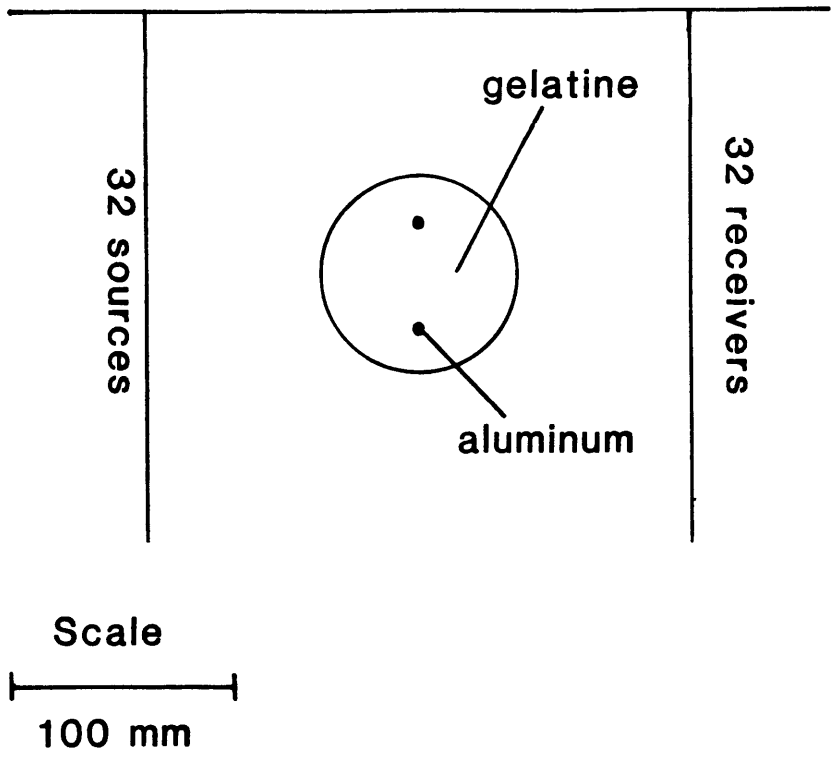

Figure 12: Experimental configuration of the cross-borehole experiment with a more complicate object. The object is a gelatin cylinder with two aluminum rods inside.

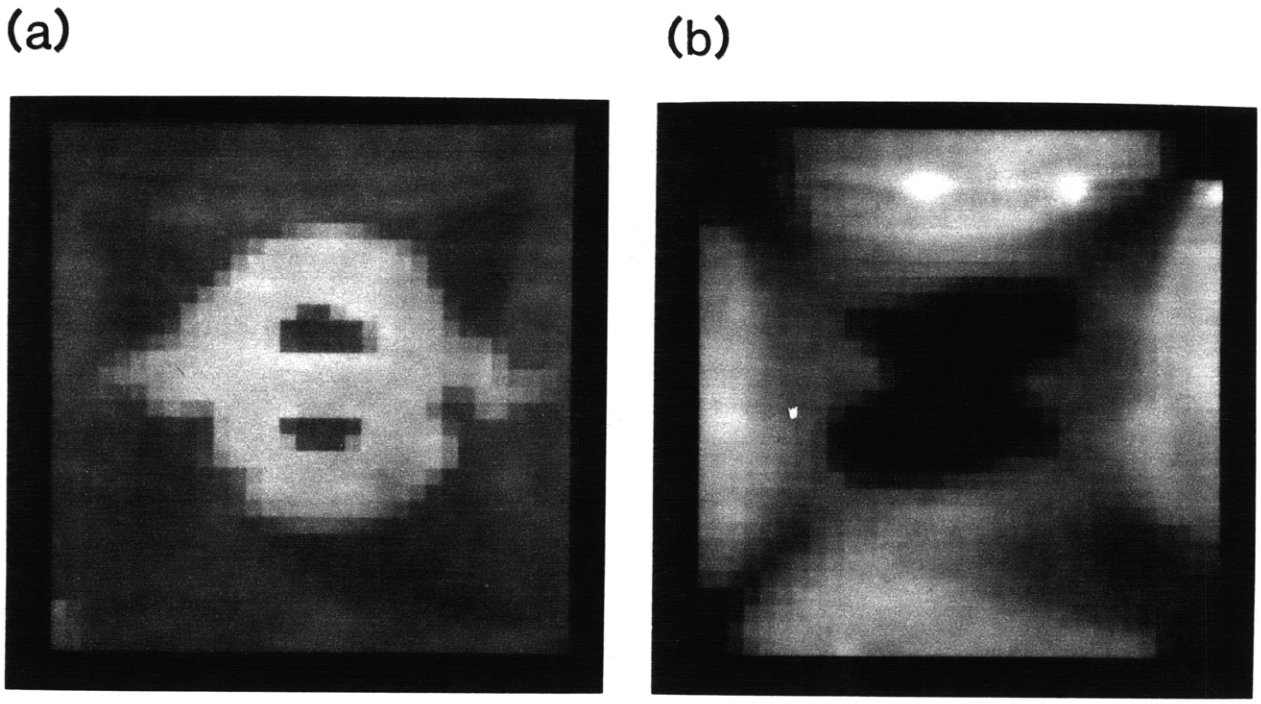

Figure 13: Images reconstructed by the filtered backpropagation and the ART algorithms for a gelatin cylinder with two aluminum rods in the cross-borehole experiment. (a) Image reconstructed by the filtered backpropagation algorithm with the Born approximation at 30 KHz. (b) Image reconstructed by the ART.

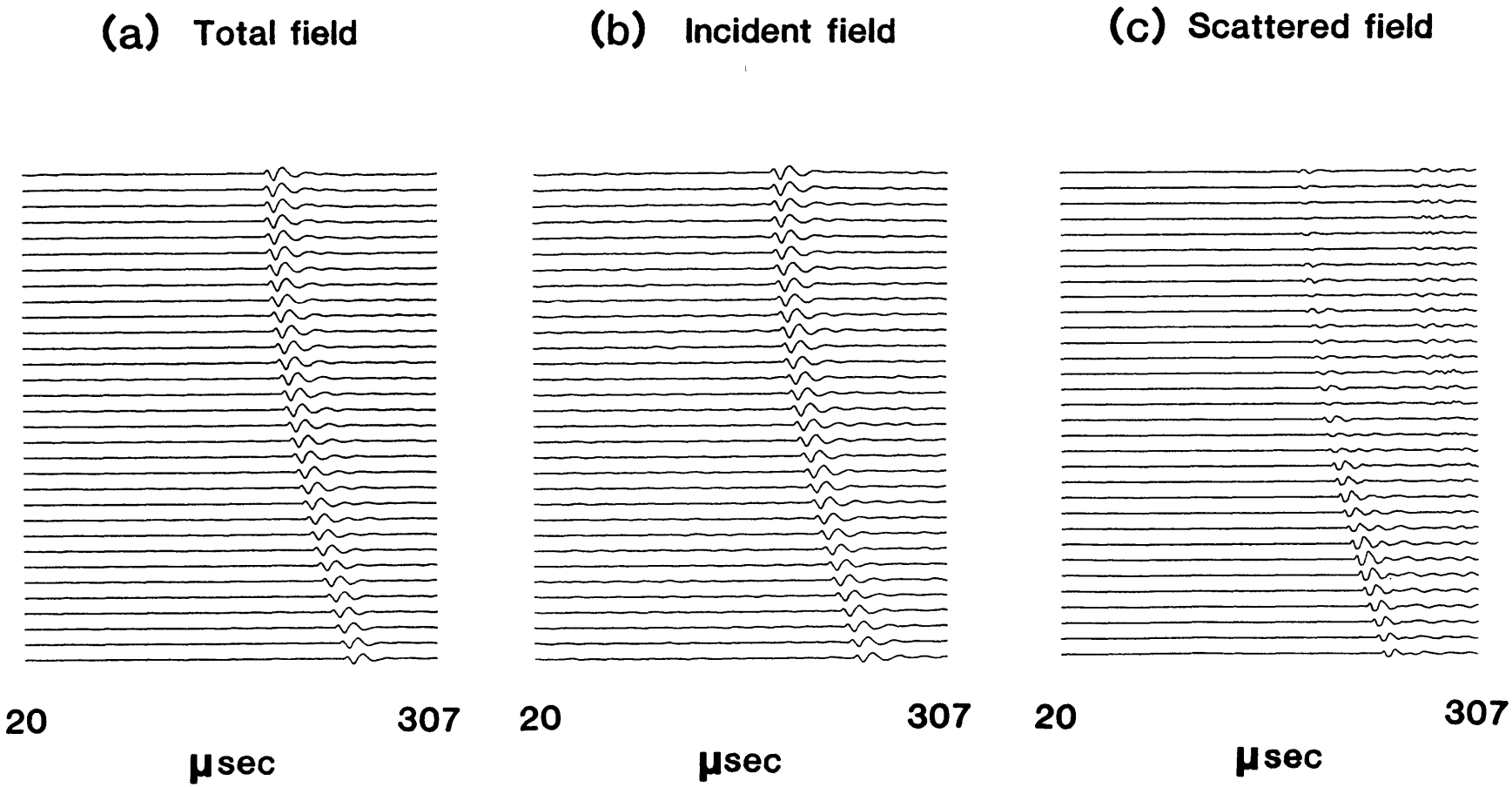

Figure 14: Examples of waveforms recorded in the VSP experiment. (a) Total field waveforms. (b) Incident field waveforms. (c) Scattered field waveforms.

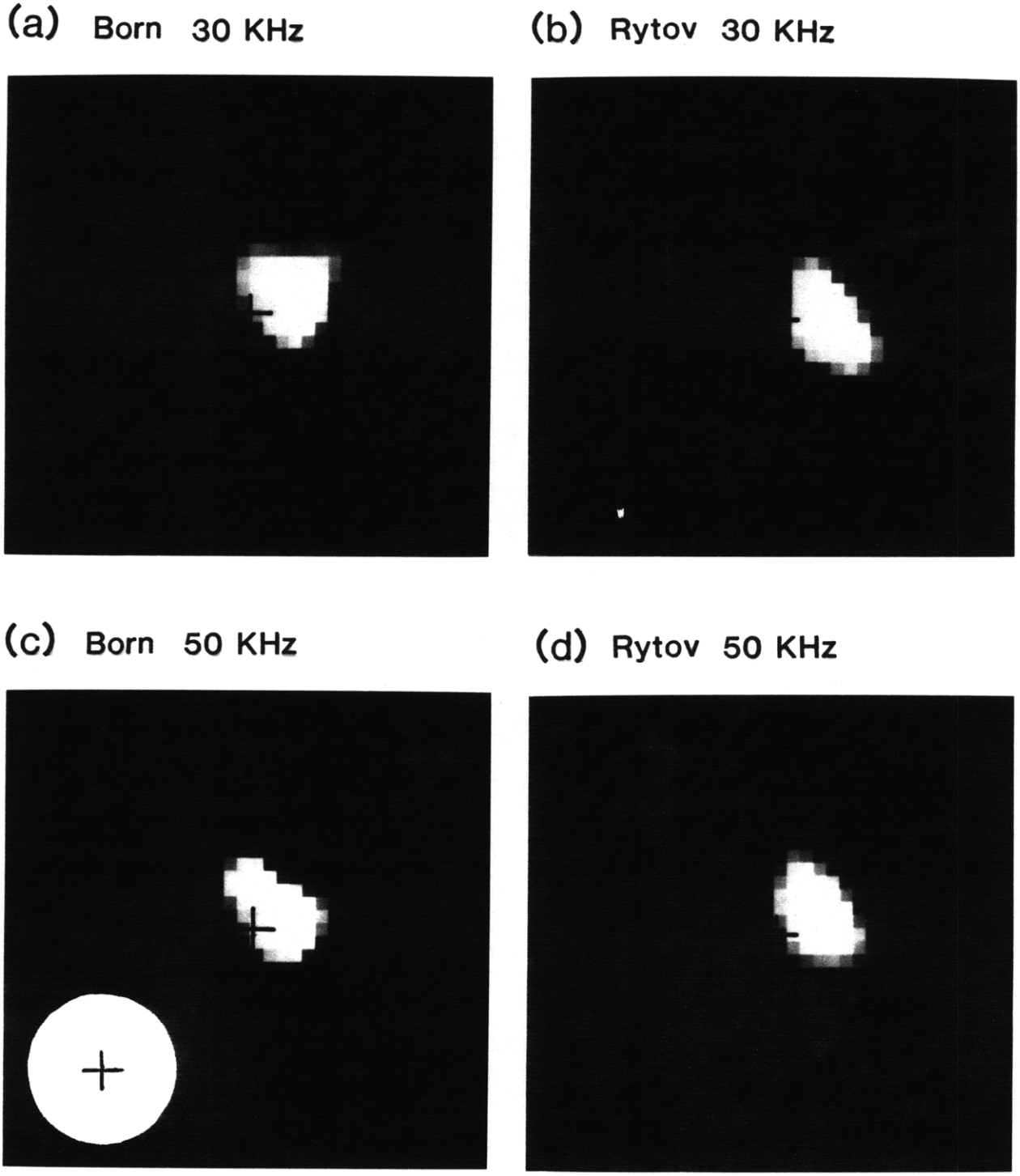

Figure 15: Images reconstructed by the filtered backpropagation algorithm in the VSP experiment. The gelatin cylinder should be centered at the cross with the size and shape as shown by the white circle at the lower left corner of the figure. (a) Reconstruction with the Born approximation at 30 KHz. (b) Reconstruction with the Rytov approximation at 30 KHz. (c) Reconstruction with the Born approximation at 50 KHz. (d) Reconstruction with the Rytov approximation at 50 KHz.

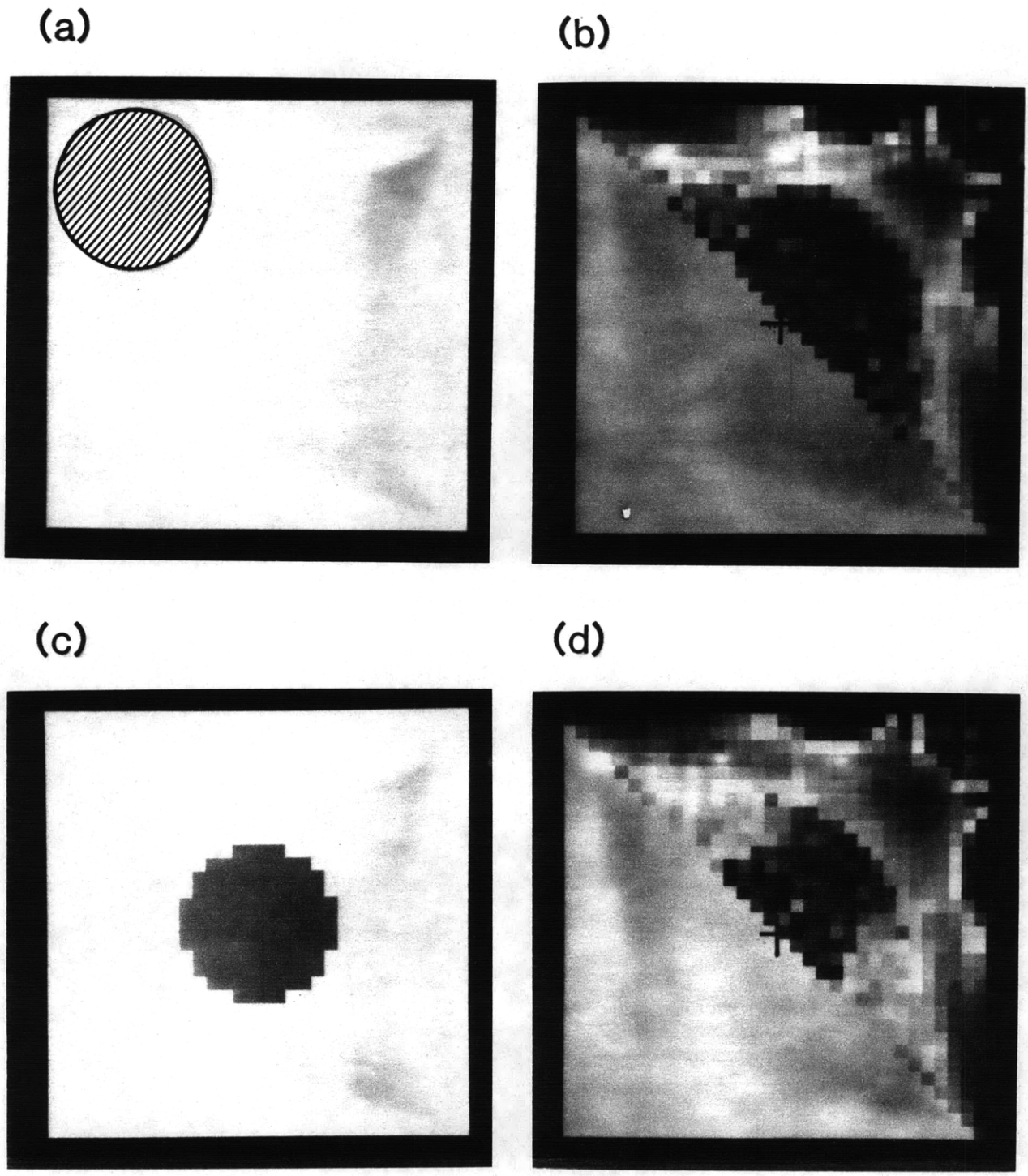

Figure 16: Images reconstructed by the ART algorithm in the VSP experiment. The gelatin cylinder should be centered at the cross with the size and shape as shown by the shaded circle at the upper left corner of the figure. (a) An initial estimate assuming no information about the object function. (b) ART reconstruction of the object with an initial estimate like (a) after six iterations. (c) An initial estimate very close to the true object function. (d) ART reconstruction of the object with an initial estimate like (c) after six iterations.

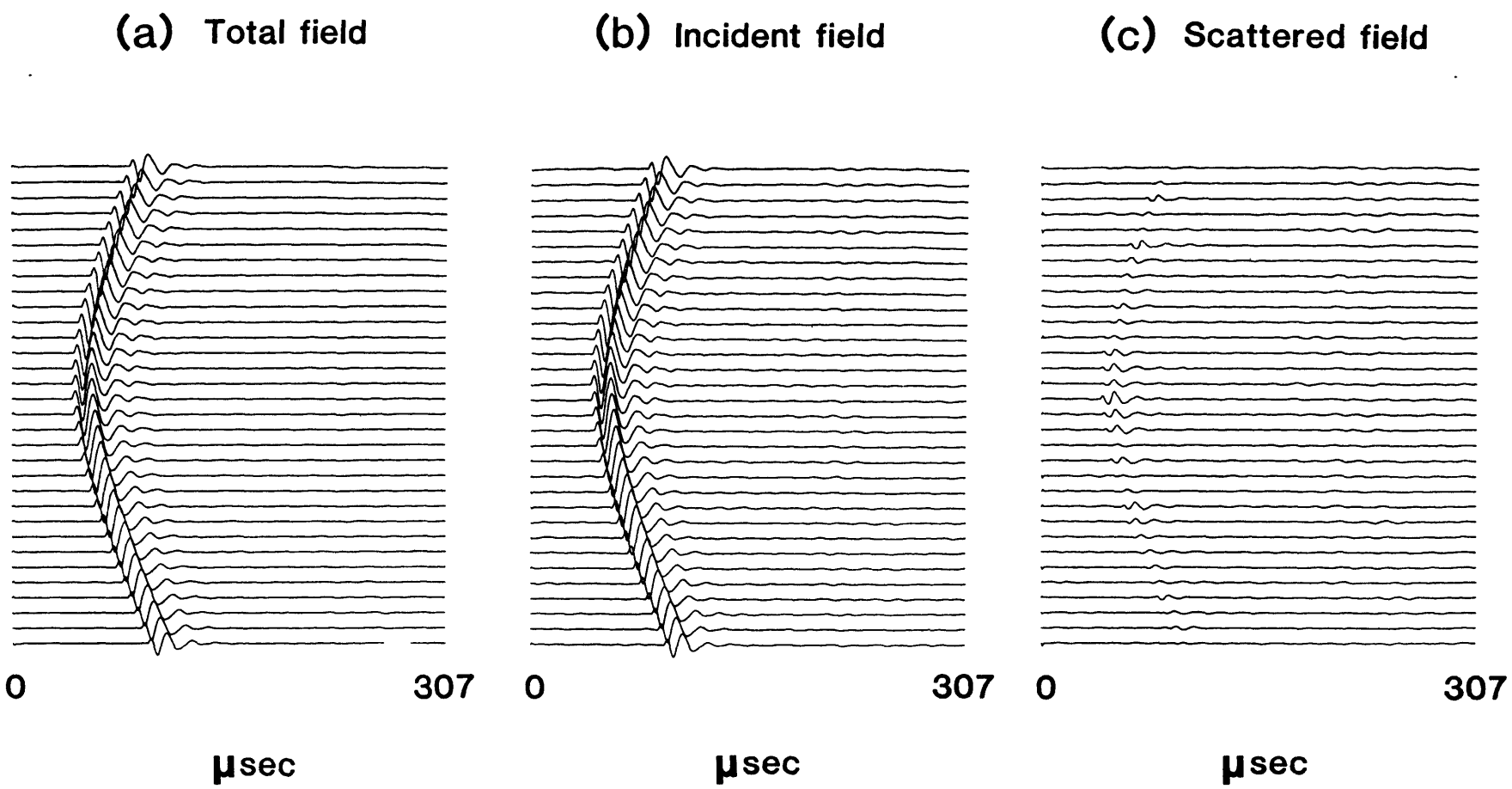

Figure 17: Examples of waveforms recorded in the surface reflection experiment. (a) Total field waveforms. (b) Incident field waveforms. (c) Scattered field waveforms.

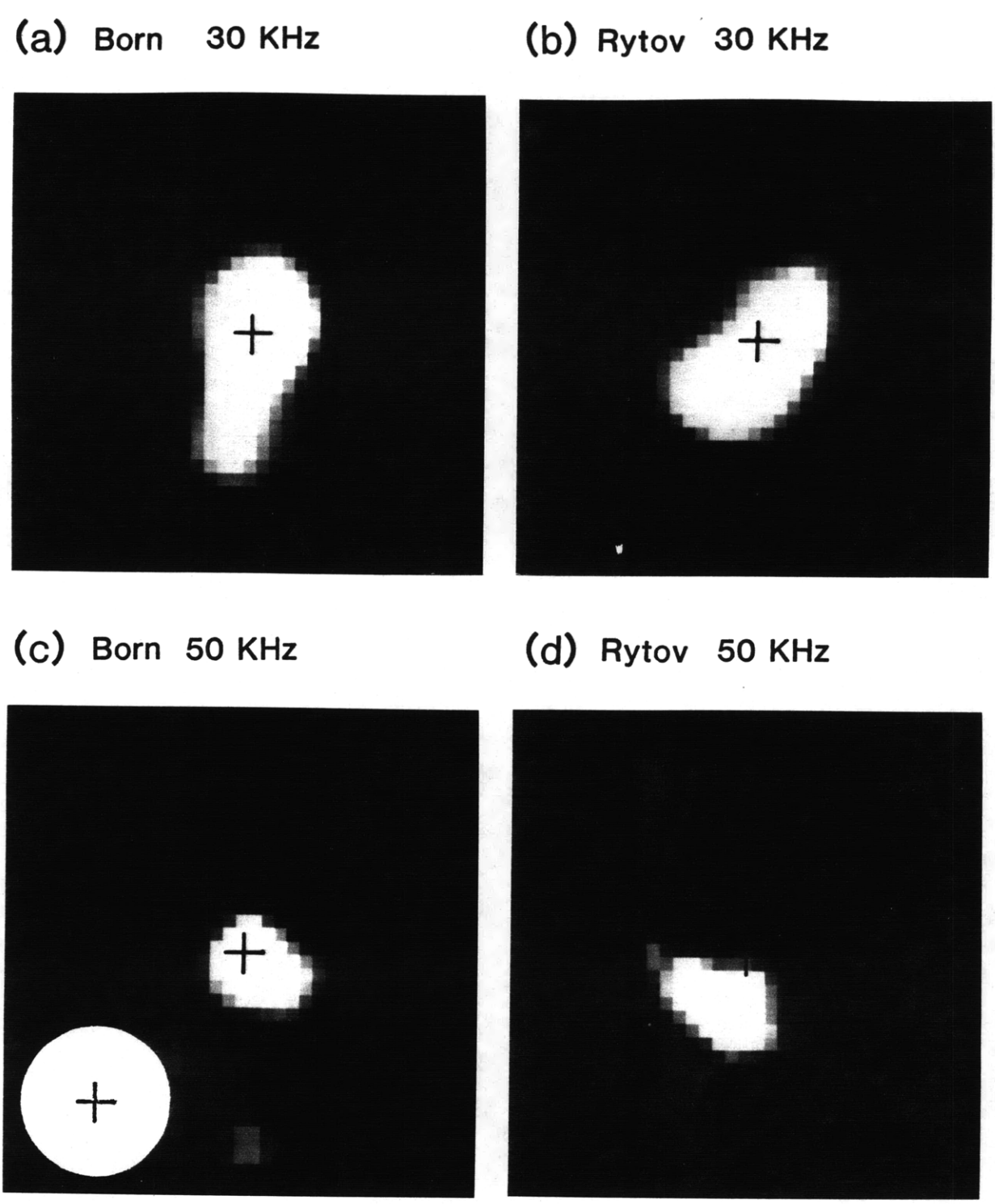

Figure 18: Images reconstructed by the filtered backpropagation algorithm in the surface reflection experiment. The gelatin cylinder should be centered at the cross with the size and shape as shown by the white circle at the left lower corner of the figure. (a) Reconstruction with the Born approximation at 30 KHz. (b) Reconstruction with the Rytov approximation at 30 KHz. (c) Reconstruction with the Born approximation at 50 KHz. (d) Reconstruction with the Rytov approximation at 50 KHz.

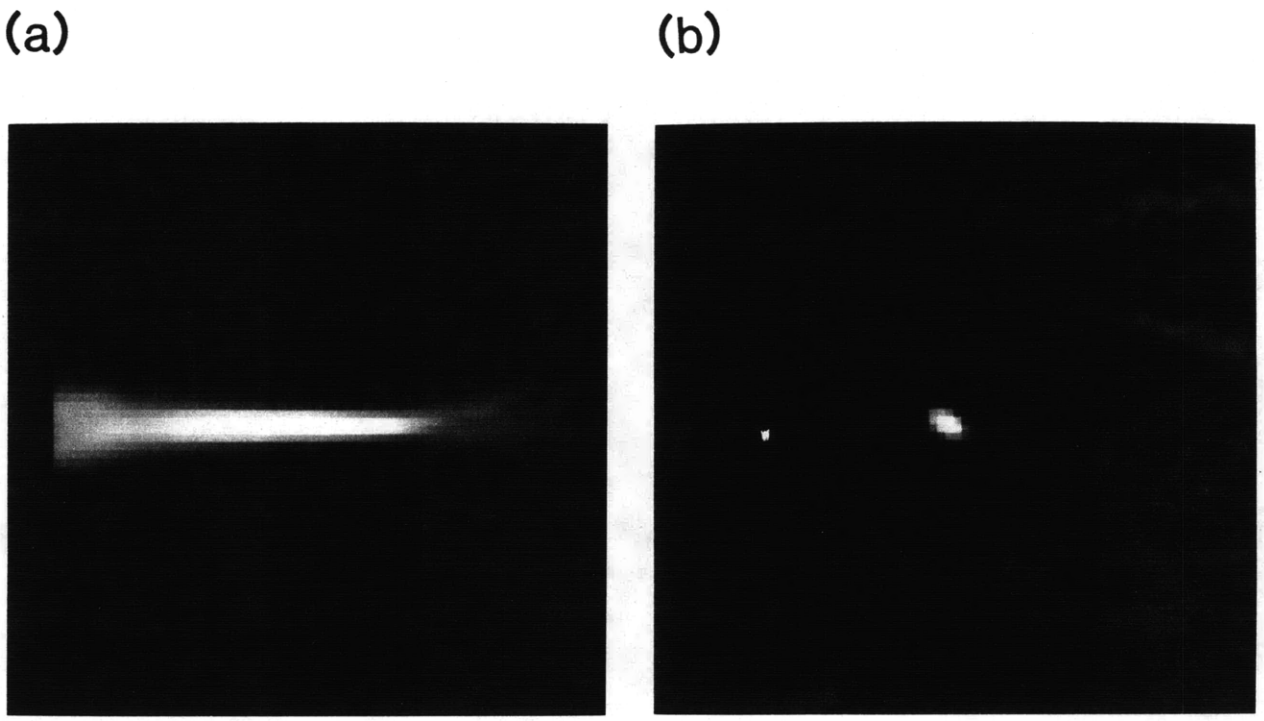

Figure 19: Holographic reconstruction of a single steel bead in the VSP experiment. (a) Reconstruction with the single frequency data at 30 KHz. (b) Multi-frequency reconstruction using ten set of data ranging from 25 KHz to 34 KHz.

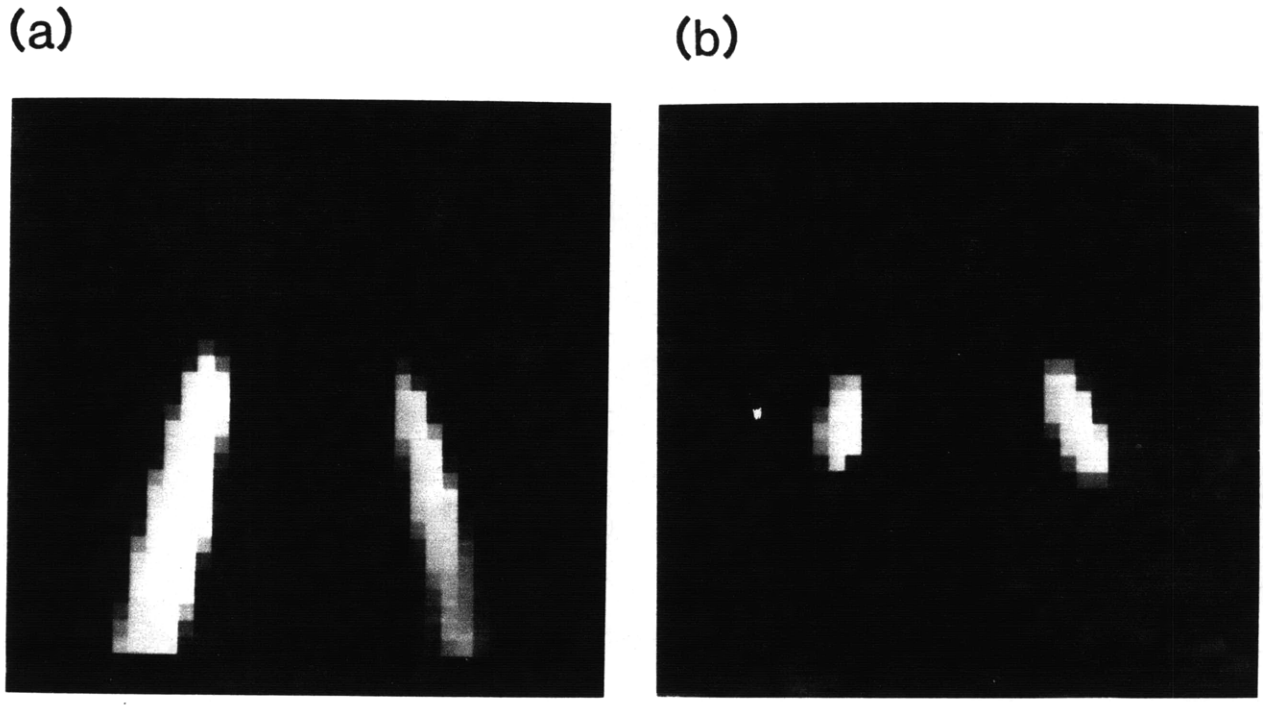

Figure 20: Holographic reconstruction of a pair of steel rods in the surface reflection experiment. (a) Reconstruction with the single frequency data at 37 KHz. (b) Multi-frequency reconstruction using three set of data ranging from 37 KHz to 44 KHz.